
1 **Markedly different impacts of primary emissions and secondary**
2 **aerosol formation on aerosol mixing states revealed by simultaneous**
3 **measurements of CCNC, V/HTDMA, and SP2**

4 Jiangchuan Tao^{1,8}, Biao Luo^{1,8}, Weiqi Xu³, Gang Zhao⁶, Hanbin Xu⁵, Biao Xue^{1,8}, Miaomiao Zhai^{1,8},
5 Wanyun Xu⁴, Huarong Zhao⁷, Sanxue Ren⁷, Guangsheng Zhou⁷, Li Liu^{2,*}, Ye Kuang^{1,8,*}, Yele Sun³

6 ¹ Institute for Environmental and Climate Research, Jinan University, Guangzhou, Guangdong, China

7 ² Key Laboratory of Regional Numerical Weather Prediction, Institute of Tropical and Marine
8 Meteorology, China Meteorological Administration, Guangzhou, China.

9 ³ State Key Laboratory of Atmospheric Boundary Layer Physics and Atmospheric Chemistry, Institute
10 of Atmospheric Physics, Chinese Academy of Sciences, Beijing, China.

11 ⁴ State Key Laboratory of Severe Weather, Key Laboratory for Atmospheric Chemistry, Institute of
12 Atmospheric Composition, Chinese Academy of Meteorological Sciences, Beijing, China

13 ⁵ Experimental Teaching Center, Sun Yat-Sen University, Guangzhou, China

14 ⁶ State Key Joint Laboratory of Environmental Simulation and Pollution Control, International Joint
15 Laboratory for Regional Pollution Control, Ministry of Education, College of Environmental Sciences
16 and Engineering, Peking University, Beijing 100871, China

17 ⁷ Hebei Gucheng Agricultural Meteorology National Observation and Research Station, Chinese
18 Academy of Meteorological Sciences, Beijing, 100081, China

19 ⁸ Guangdong-Hongkong-Macau Joint Laboratory of Collaborative Innovation for Environmental
20 Quality, Jinan University, Guangzhou, Guangdong, China

21 Correspondence: Ye Kuang (kuangye@jnu.edu.cn), Li Liu (liul@gd121.cn)

22

23 **Abstract**

24 ~~The aerosol mixing state is a crucial physicochemical property that affects the optical properties and~~
25 ~~cloud condensation nuclei (CCN) activity. Multiple techniques are commonly employed to determine~~
26 ~~the aerosol mixing states for various applications, and comparisons between these techniques provide~~
27 ~~insights into the variations in aerosol chemical and physical properties. These techniques include size-~~
28 ~~resolved CCN activity measurements using a system with a CCN counter (CCNC) coupled with a~~
29 ~~differential mobility analyzer (DMA), a Humidified/Volatility Tandem Differential Mobility Analyzer~~
30 ~~(H/V-TDMA) that measures aerosol hygroscopicity and volatility distributions, and a single particle~~
31 ~~soot photometer (SP2) that directly quantifies black carbon (BC) mixing states. This study provides~~
32 ~~the first comparison of~~compares ~~aerosol mixing state parameters obtained~~ through~~via~~ simultaneous
33 measurements using DMA-CCNC, H/V-TDMA, and DMA-SP2. ~~The, shedding light on the~~
34 ~~impacts of primary aerosol emissions and secondary aerosol (SA) formation on the aerosol mixing~~
35 ~~states and the intercomparison results were analyzed. The results showed that the differences in the,~~
36 The analysis reveals significant variations in ~~mixing-state parameters~~ measured using among ~~different~~
37 ~~techniques varied significantly under different conditions. The,~~ with ~~V-TDMA and DMA-SP2~~
38 ~~measurements showed~~indicating ~~that the non-volatile population identified by V-TDMA was particles~~
39 ~~mainly contributed by the~~stem from ~~BC-containing aerosols. H/TDMA and DMA-SP2 measurements~~
40 ~~indicated that, while~~ a substantial proportion of nearly hydrophobic aerosols ~~did not originate from~~
41 ~~BC-containing aerosols but likely originated~~originates ~~from fossil fuel combustion and biomass-~~
42 ~~burning emissions. The synthesized comparison results between the DMA-CCNC, H/TDMA, and~~
43 ~~DMA-SP2 measurements revealed that~~Synthesizing the results, ~~some nearly hydrophobic BC-free~~
44 ~~particles were~~ found to be ~~CCN-inactive under supersaturated conditions, likely from fossil fuel~~
45 ~~combustion emissions. In contrast, while~~ others were CCN-active under supersaturated conditions,
46 ~~linked to biomass-~~burning emissions. Moreover, ~~BC-containing aerosols emitted from fossil fuel~~
47 ~~combustion~~ tend to be~~exhibit~~ more ~~externally mixed~~external mixing ~~with other aerosol components~~
48 ~~than compared to those emitted by~~from ~~biomass-~~burning activities. These results highlight significant
49 ~~disparities in the mixing states and physicochemical properties of aerosols from fossil fuel and biomass~~
50 ~~burning. The formation of secondary. Secondary~~ nitrate and organic aerosolsaerosol formation
51 ~~significantly~~ affects ~~variations in~~ affect ~~aerosol mixing states,~~ generally ~~enhancing aerosol~~

52 hygroscopicity and volatility while reducing ~~differences in mixing state parameters derived from~~
53 ~~different techniques, reducing aerosol~~ heterogeneity. ~~Variations in the number of BC-free particle~~
54 ~~fractions showed that SAs tended to form more quickly on BC-free particles than on BC-containing~~
55 ~~particles. Further comparison of the mixing state parameters revealed that the among techniques. The~~
56 ~~study also highlights distinct physical properties of~~ two resolved secondary organic aerosol factors ~~in~~
57 ~~this study exhibited remarkably different, hinting at formation through different mechanisms. These~~
58 ~~findings underscore the importance of comparing aerosol mixing states from different techniques as a~~
59 ~~tool in understanding aerosol~~ physical properties, ~~indicating that they likely formed through different~~
60 ~~pathways. These findings suggest that comparisons among aerosol mixing states derived~~ from different
61 ~~techniques can provide deeper insights into the physical properties of aerosols and how they are~~
62 ~~affected by sources and their responses to~~ SA formation, ~~as well as aiding in the~~
63 ~~investigation~~ exploration of SA formation ~~pathways.~~ mechanisms.

64 1 Introduction

65 The aerosol mixing state is a crucial physicochemical property of aerosol particles (Riemer et al.,
66 2019), exerting a significant impact on their optical properties and cloud condensation nuclei (CCN)
67 activity, thus affecting their impact on the climate and environment (Fierce et al., 2017; Riemer et al.,
68 2019; Stevens et al., 2022). For example, variations in the mixing state of black carbon (BC) particles
69 can significantly alter their absorption and radiative effects (Bond et al., 2013; Lack et al., 2012; Zhao
70 et al., 2019; Moffet et al., 2016; Matsui et al., 2018; Peng et al., 2016). Using simple internal mixing
71 state assumptions for aerosol chemical compositions components to estimate CCN number
72 concentrations can lead to substantial overestimations (up to 30%; Deng et al., 2013; Farmer et al.,
73 2015; Ren et al., 2018; Ching et al., 2017, 2019; Tao et al., 2021). The aerosol mixing state varies
74 widely due to complex emissions and atmospheric transformations, leading to significant uncertainties
75 in estimating the effects of aerosols based on simplified mixing state assumptions (Ervens, 2015; Wang
76 et al., 2022; Fu et al., 2022).

77 The aerosol mixing state describes the mixture of aerosol chemical components within each
78 particle and the distribution of these particles in the aerosol population. This property can be directly
79 measured using single-particle chemical composition techniques (Fierce et al., 2017; Riemer et al.,
80 2019), such as the single-particle soot photometer (SP2), which measures refractory black carbon (rBC)
81 mass concentrations and the mixing state of rBC with other aerosol components, or single-particle
82 chemical composition measurement techniques (e.g., single-particle aerosol mass spectrometer, SP-
83 AMS) that have been developed in recent years (Lee et al., 2019; Riemer et al., 2019 and reference
84 therein). Alternatively, the aerosol mixing state can be inferred from indirect measurements of aerosol
85 properties, such as size-resolved aerosol CCN activity (measured by coupling a differential mobility
86 analyzer (DMA) and a CCN counter (CCNC)), size-resolved aerosol hygroscopicity distributions, or
87 volatility distributions (measured by a Humidified/Volatility Tandem differential mobility analyzer
88 (H/V-TDMA)).

89 However, each technique yields information on aerosol mixing states based on different aerosol
90 microphysical properties, thus obtaining aerosol mixing states that are different but linked to one
91 another. For instance, while both CCN activity and hygroscopic growth measurements are associated
92 with aerosol hygroscopicity, an intercomparison between CCNC and HTDMA measurements has

93 prompted investigations into aerosol hygroscopicity variations under different saturation conditions
94 (Su et al., 2010; Juranyi et al., 2013; Lance et al., 2013; Kawana et al., 2016; Tao et al., 2020; Jiang et
95 al., 2021). Although the SP2 and VTDMA techniques depend on the evaporation of non-refractory
96 compositions, only rBC remains in the SP2 measurements. In contrast, non-refractory composition
97 evaporation depends on the thermodynamic temperature in the VTDMA measurements. Thus,
98 measurements of an SP2 are highly correlated to those of a VTDMA at high temperatures (200 °C–
99 300 °C), with their differences reflecting variations in aerosol density, shape, or volatility (Philippin
100 et al., 2004; Wehner et al., 2009; Adachi et al., 2018, 2019; Wang et al., 2022). HTDMA and VTDMA
101 can be combined to study the influence of the aerosol mixing state on hygroscopicity and volatility
102 (Zhang et al., 2016; Cai et al., 2017; Wang et al., 2017). Strong correlations were found between the
103 hydrophobic and non-volatile particles, suggesting they might have similar chemical compositions
104 (Zhang et al., 2016). In addition, some studies have shown that, except for BC, low-volatility particles
105 correlate well with CCN-inactive particles based on VTDMA and CCNC measurements (Kuwata et
106 al., 2007; Kuwata and Kondo, 2008; Rose et al., 2011; Cheng et al., 2012). Therefore,
107 intercomparisons between mixing state parameters measured by distinct techniques provide a better
108 characterization of the aerosol mixing state and insight into aerosol physiochemical properties.
109 Previous studies have mainly compared two types of aerosol mixing state measurements and lacked a
110 comprehensive comparative analysis among SP2, DMA-CCN, and HV-TDMA measurements,
111 hindering the wide application of derived aerosol mixing states obtained by individual techniques.

112 The mixing state of primary aerosols can vary greatly depending on their type and emission
113 conditions (Cheng et al., 2012; Wang et al., 2017; Wang et al., 2022; Ting et al., 2018; Liu et al., 2021)
114 and can be significantly altered during aging processes or secondary formations (Wehner et al., 2009;
115 Cheng et al., 2012; Wang et al., 2022; Tomlin et al., 2021; Lata et al., 2021). Primary aerosol emissions,
116 such as biomass burning, fossil fuel combustion, and cooking, tend to contribute to weak
117 hygroscopicity (Herich et al., 2008, 2009; Wang et al., 2020; Kim et al., 2020) and low-volatility
118 aerosols (Hong et al., 2017; Saha et al., 2018). The formation of secondary aerosols (SAs), including
119 the aging of BC-containing [aerosol particles](#) and primary organic aerosols, mainly contributes to
120 aerosols with strong CCN activity (Mei et al., 2013; Ma et al., 2016; Tao et al., 2021) and high
121 hygroscopicity (Chen et al., 2018; Kim et al., 2020; Wang et al., 2020). It is important to study the

122 impact of specific primary aerosol emissions and SA formation on aerosol mixing states and the
123 influence of aerosol mixing state parameters derived from different techniques to enhance our
124 understanding of the mixing state of aerosols from different emission sources and improve their
125 characterization in models.

126 The North China Plain (NCP) is among the most polluted regions in China, with various primary
127 emission sources and strong SA formations that play critical roles in air pollution (Xu et al., 2011; Tao
128 et al., 2012; Liu et al., 2015). The complex mixing state of aerosols in the NCP contributes to
129 uncertainties in evaluating their climate and environmental effects (Zhuang et al., 2013; Nordmann et
130 al., 2014; Zhang et al., 2016; Tao et al., 2020; Shi et al., 2022), particularly regarding BC particles
131 (Wu et al., 2017; Liu et al., 2019; Zhao et al., 2019; Wang et al., 2011; Zheng et al., 2019).
132 Meteorological conditions can greatly affect SA formation in the NCP and can be significantly
133 exacerbated during severe pollution events. SA formation under low relative humidity (RH) conditions,
134 mainly through the condensation of gaseous-phase oxidation products, would change to that mainly
135 occurring in the aqueous phase under high RH conditions (Kuang et al., 2020). Because SAs formed
136 through different mechanisms, have different chemical compositions and add mass to different aerosol
137 populations, SA formation under different meteorological conditions can affect the aerosol mixing
138 states differently (Tao et al., 2021). This study obtained the aerosol mixing state through concurrent
139 measurements of the CCN activity, hygroscopicity, volatility, and BC particles at a regional site in the
140 NCP using CCNC, HTDMA, VTDMA, and SP2 instruments. This provides a unique opportunity to
141 perform a comprehensive inter-comparison of the aerosol mixing states among different techniques to
142 gain insight into the impact of primary aerosol emissions and SA formation on the observed aerosol
143 mixing states.

144

145 **2 Materials and methods**

146 **2.1 Campaign information and instruments setup**

147 From the 16th of October to the 16th of November 2021, aerosol mixing states were continuously
148 and concurrently monitored using different techniques at the Gucheng site in Dingxing County, Hebei
149 Province, China, as part of a campaign to investigate Aqueous Secondary ~~aerosol-formation~~aerOsol
150 Formation in ~~fog~~Fog and ~~aerosols~~Aerosols and their ~~radiative~~Radiative effects in the NCP (AQ-

151 SOFAR). The observation site, located at 39°09'N, 115°44'E, is an Ecological and Agricultural
152 Meteorology Station of the Chinese Academy of Meteorological Sciences, situated between the
153 megacities of Beijing (approximately 100 km away) and Baoding (approximately 40 km away) and
154 surrounded by farmlands and small towns. This site provides a representative view of the background
155 atmospheric pollution conditions in the NCP (Kuang et al., 2020; Li et al., 2021).

156 Different measurement techniques were used to simultaneously obtain the aerosol mixing state
157 through CCN activity, hygroscopicity, volatility, and BC particle observations. In addition to aerosol
158 mixing state measurements, the AQ-SOFAR campaign includes measurements of aerosol number size
159 distribution, chemical composition, aerosol scattering, and absorption properties. Aerosol number size
160 distributions in the diameter range of 13 nm–4 μm were measured by the scanning mobility particle
161 sizer (13–550 nm) and the aerodynamic aerosol classifier (100 nm–4 μm), and they are merged by
162 assuming an aerosol density of 1.6 g/cm³. The total BC mass concentrations were determined using an
163 aethalometer (Magee, AE33; Drinovec et al., 2015); more information on the correction of absorption
164 measurements and mass concentration calculations is available in Luo et al. (2022). All aerosol
165 measurement instruments were housed in a temperature-controlled container at 24 °C. The inlet was
166 switched among three impactors: TSP (Total Suspended Particles), PM_{2.5} (Particulate Matter with an
167 aerodynamic diameter of less than 2.5 μm), and PM₁ (Particulate Matter with an aerodynamic diameter
168 of less than 1 μm). Inlet changes among impactors affect dry-state aerosol sampling owing to ambient
169 aerosols are enlarged through aerosol hygroscopic growth or activation. However, the aerosol mixing
170 state and aerosol chemical composition measurements were made on submicron aerosols, and the inlet
171 change almost did not affect those measurements under conditions of RH less than 90%. The sampled
172 aerosol was dried by two parallelly assembled Nafion dryers with a length of 1.2 m. Two Nafion driers
173 ~~was~~ used because of the high RH and sample flow rate (~16 L/min) during the campaign to ensure
174 drying efficiency. The flow rate is carefully adjusted in the inlet in order to ensure accurate aerosol
175 particle size cutoff. In addition, during autumn and winter in the NCP, ambient air temperature (<20 °C
176 and sometimes <0 °C) can be significantly lower than the room temperature (~24 °C). Therefore, this
177 dryer system can maintain the RH of sampled aerosols to below 20%. Meteorological data such as
178 temperature, pressure, wind speed, wind direction, and RH were obtained from an automatic weather
179 station operated by the station.

180 The chemical composition of the submicron aerosols was analyzed using a High-Resolution
181 Time-of-Flight Aerosol Mass Spectrometer (HR-ToF-AMS). The ionization efficiency (IE) was
182 calibrated using 300 nm diameter pure NH_4NO_3 particles, following the standard protocols outlined in
183 Jayne et al. (2000) in the middle of the campaign, with the relative ionization efficiency (RIE) of
184 ammonium determined to be 5.26. The RIE of sulfate was 1.28 using pure $(\text{NH}_4)_2\text{SO}_4$ particles, and
185 the default RIEs of 1.4 for organic aerosols, 1.1 for nitrates, and 1.3 for chlorides were used as the
186 organic aerosols. The composition-dependent collection efficiency reported by Middlebrook et al.
187 (2012) was used. Elemental ratios were derived using the “Improved-Ambient (I-A)” method as
188 described in Canagaratna et al. (2015), including hydrogen to carbon (H/C), oxygen to carbon (O/C),
189 and organic mass to organic carbon (OM/OC) ratios. Two primary organic aerosol (POA) and two
190 oxygenated organic aerosol (OOA) factors were identified by High-Resolution Positive Matrix
191 Factorization (HR-PMF; Ulbrich et al., 2009; Paatero and Tapper, 1994). This study used the
192 summation of the two OOA factors to represent secondary organic aerosols (SOA). The mass spectra
193 of the organic aerosol (OA) factors and their correlations with external species are shown in Figs. S1
194 and S2. The Biomass Burning Organic Aerosol (BBOA) spectrum was characterized by
195 ~~obvious~~ abundant fragments of m/z 60 (mainly $\text{C}_2\text{H}_4\text{O}_2^+$) and 73 (mainly $\text{C}_3\text{H}_5\text{O}_2^+$), two indicators of
196 biomass burning (Mohr et al., 2009). BBOA correlated well with $\text{C}_2\text{H}_4\text{O}_2^+$ ($R^2=0.91$) and $\text{C}_3\text{H}_5\text{O}_2^+$
197 ($R^2=0.90$). Consistent with previous studies in Beijing (Xu et al., 2019), the PMF analysis revealed a
198 mixed factor named Fossil Fuel Organic Aerosol (FFOA), which comprises traffic emissions and coal
199 combustion and is characterized by a typical hydrocarbon ion series. FFOA had a relatively high f_{44}
200 (0.083) value, which was likely due to aging during regional transportation, similar to the results
201 observed in the winter of 2016 in Beijing (Xu et al., 2019) and coal combustion organic aerosols in
202 Gucheng (Chen et al., 2022). Secondary organic aerosol formation from volatile organic compound
203 precursors could occur in different formation pathways, such as aqueous-phase, heterogeneous, or gas-
204 phase reactions. It might also be oxidized under different conditions, such as oxidation under different
205 nitrogen oxide conditions with different oxidation capacities and oxidants. The two resolved OOA
206 factors displayed different spectral patterns, correlations with tracers, and diurnal variations,
207 suggesting that they resulted from different chemical processes. However, their formation mechanisms
208 remain to be explored in future studies. In general, the OOA factor 1 (OOA1) has higher $\text{CO}_2^+/\text{C}_2\text{H}_3\text{O}^+$
209 (3.9) and O/C (0.91) ratios than OOA factor 2 (OOA2) with 2.1 and 0.78, respectively.

210 This study did not consider losses in the inlet line and sampling systems for the following
211 reasons: (1) investigated mixing state parameters are represented by number fractions (NFs) of
212 different diameters, which are much less affected by losses in sampling systems compared with
213 absolute number concentrations; and (2) good consistency was achieved between measurements of
214 particle number size distributions (PNSD) and mass concentrations measured by AMS. The average
215 ratio between volume concentration derived from AMS and rBC measurements (densities of
216 compounds are the same as Kuang et al., 2021) and the volume concentration derived from PNSD
217 measurements was 0.79 ($R=0.97$, as shown in Fig. S3), consistent with previous reports as AMS cannot
218 detect aerosol components, such as dust (Kuang et al., 2021).

219 **2.2 Aerosol mixing states measurement techniques**

220 **2.2.1 DMA-CCNC measurements**

221 The CCN activity of the particles under supersaturated conditions was measured using a DMA-
222 CCNC system, which consisted of a differential mobility analyzer (DMA; model 3081, TSI, Inc., MN,
223 USA), condensation particle counter (CPC; model 3756, TSI, Inc., MN, USA), and continuous-flow
224 CCNC (model CCN100, Droplet Measurement Technologies, USA). The system was operated in size-
225 scanning mode and provided the Size-resolved Particle Activation Ratio (SPAR) by combining CPC
226 and CCNC measurements at different particle sizes. To compare the instruments, three
227 supersaturations (SSs) of 0.08%, 0.14%, and 0.22% were applied in a single cycle of approximately
228 15 min. CCN measurements under these three SSs revealed that the CCN activity of aerosols resides
229 in the accumulation mode with an aerosol diameter range of approximately 100–200 nm, which is
230 close to the diameters of the HV-TDMA measurements. Higher SSs would reveal CCN activities of
231 smaller aerosol particles (<100 nm), where the DMA-SP2 measurement is unavailable. The sample
232 and sheath flow rates of DMA were set at 1 and 5 lpm, respectively, resulting in a measured particle
233 diameter range of 9–500 nm, with a running time of 5 min per cycle. Supersaturation in the CCNC
234 was calibrated with monodisperse ammonium sulfate particles (Rose et al., 2008) before and after the
235 campaign. The flow rates were also calibrated before and after the campaign and checked daily to
236 minimize uncertainties in droplet counting and supersaturation formed in the column (Roberts and
237 Nenes, 2005; Lance et al., 2006). SPAR deviations due to multiple-charge particles were corrected

238 using a modified algorithm based on Hagen and Alofs (1983) and Deng et al. (2011). Further details
239 regarding this system can be found in Ma et al. (2016) and Tao et al. (2021).

240 2.2.2 H/V-TDMA measurements

241 The mixing state of the aerosols in terms of hygroscopicity and volatility was measured using a
242 Hygroscopicity/Volatility Tandem Differential Mobility Analyzer (H/V-TDMA; Tan et al., 2013). The
243 H/V-TDMA consisted of two DMA (Model 3081 L, TSI Inc.), with the first DMA (DMA1) selecting
244 dried particles without conditioning (RH ~15%) and the second DMA (DMA2) selecting conditioned
245 particles. H/V-TDMA can operate in either H- or V-mode, controlled by a three-way solenoid valve.
246 A Nafion humidifier was used in the H-mode to condition the selected dry particles to 90% RH
247 equilibrium. The number-size distribution of humidified particles (D_p) was measured using DMA2 and
248 CPC (Model 3772, TSI Inc.). The RH-dependent hygroscopic growth factor (GF) at a specific diameter
249 (D_d) was calculated as follows:

$$250 \quad GF = \frac{D_p(RH)}{D_d} \quad (1)$$

251 where $D_p(RH)$ is the size of particles undergoing humidification. Four dry electrical mobility diameters
252 (50, 100, 150, and 200 nm) were measured in this mode. The instrument was regularly calibrated using
253 standard polystyrene latex spheres (PSL) and ammonium sulfate particles.

254 In V-mode, a heated tube evaporated the volatile coatings from the previously selected dry
255 particles. Six temperature settings were used for the heated tube, ranging from 25–200°C. The number-
256 size distributions of the heated particles were measured using DMA2 and CPC. In addition to the four
257 particle sizes measured in the H-mode, three additional particle sizes (250, 300, and 350 nm) were
258 measured in the V-mode (residence time inside the heated tube to be about 1.6 s; Hong et al., 2017).
259 The temperature-dependent shrinkage factor (SF), which is the ratio of heated particle size to dry
260 particle size without heating (D_d), is defined as:

$$261 \quad SF = \frac{D_p(T)}{D_d} \quad (2)$$

262 where $D_p(T)$ denotes the particle diameter during heating. A complete cycle of H-mode
263 measurements under one RH condition and V-mode measurements at six temperatures took
264 approximately 3 h. The Probability Density Function (PDF) of the GF (or SF) was calculated from the

265 measured density function using the inversion algorithm described by Stolzenburg and McMurry
266 (2008).

267 **2.2.3 DMA-SP2 measurements**

268 The size-resolved BC mixing states were measured using an SP2 (Droplet Measurement
269 Technology, Inc., USA) after DMA (Model 3081, TSI, USA). The DMA selected aerosols of various
270 dry particle sizes, which were then introduced into SP2. The DMA-SP2 setup was able to measure the
271 mixing states of aerosols with diameters (detection limit of approximately 80 nm based on the
272 calibration) of 100, 120, 160, 200, 235, 270, 300, 335, 370, 400, 435, 470, 500, 535, 570, 600, 635,
273 670, and 700 nm within 20 min when it was not placed after an ~~enunderenunder~~-bypass switch system
274 (during the following time periods: the 13th to the 24th of October, 09:00 am of the 5th of November
275 to 09:00 am of the 8th of November). However, it only measured mixing states at diameters of 120,
276 160, 200, 250, 300, 400, and 500 nm when it was placed after a thermodenuder-bypass switch system
277 (during the following time periods: 11:00 am of the 24th of October to 08:00 am of the 5th of
278 November, and 09:00 am of the 8th of November to 06:00 pm of the 17th of November). Because the
279 HTDMA and VTDMA measurements were conducted solely by a single H/VTDMA system operating
280 in different modes, the time needed for a single particle size measurement of HTDMA and VTDMA
281 was much longer than that of the DMA-SP2 system. Thus, for the same measurement cycle (2h), more
282 particle sizes were selected in the DMA-SP2 system ~~for acquiringto acquire~~ the BC mass concentration
283 and mixing state at larger diameters than HTDMA and VTDMA.

284 The SP2 chamber had a continuous Nd:YAG laser beam with a wavelength of 1064 nm. The BC-
285 containing particles passing through the laser beam ~~becamebecome~~ incandescent by absorbing
286 radiation. The mass concentration of the BC was calculated by measuring the intensity of the emitted
287 incandescent light. The sheath flow/sample flow ratio was maintained at 10 for the DMA to reduce the
288 width of the diameter distribution of the selected monodisperse aerosols. Additionally, the flow rate
289 of the SP2 was changed from 0.1 to 0.12 L/min starting on the 22nd of October (allowed flow rate
290 range of SP2: 0.03–0.18 L/min from the specification). SP2 was calibrated using quadrag soot particles,
291 as reported by Gysel et al. (2011). Further details regarding the calibrations are provided in Section 1
292 of the Supplementary Information.

293 **2.3 Derivations of mixing state parameters**

294 2.3.1 Fitting SPAR curves measured by the DMA-CCNC system

295 The SPAR curves were parameterized using a sigmoidal function with three parameters. As
296 shown in Fig. S4, a sigmoidal curve generally characterized the measured SPAR. This
297 parameterization assumes that the aerosol is an external mixture of CCN-active hydrophilic and CCN-
298 inactive hydrophobic particles (Rose et al., 2010). The formula used to parameterize the SPAR ($R_a(D_d)$)
299 for a specific SS is as follows (Rose et al., 2008):

$$300 \quad R_a(D_d) = \frac{\text{MAF}}{2} \left(1 + \operatorname{erf} \left(\frac{D_d - D_a}{\sqrt{2\pi}\sigma} \right) \right) \quad (7)$$

301 where erf denotes the error function. The Maximum Activation Fraction (MAF) is an asymptote of the
302 measured SPAR curve for large particles, as shown in Fig. S4, representing the number fraction of
303 CCNs relative to the total number of particles. D_a is the midpoint activation diameter, is linked to the
304 hygroscopicity of the CCNs, and indicates the diameter where the SPAR equals half of the MAF value.
305 The σ is the standard deviation of the cumulative Gaussian distribution function and characterizes the
306 heterogeneity of CCN hygroscopicity. In Fig. S4, the σ indicates the slope of the steep increase in the
307 SPAR curves when the diameter is close to D_a . Generally, hydrophilic particles larger than D_a can
308 become CCN. Therefore, these three parameters can be used to characterize the hygroscopicity of these
309 hydrophilic particles. This study did not consider the impact of nearly hydrophobic particles on SPAR,
310 as deviations from this parameterization scheme due to this impact were negligible at low SSs, as
311 stated in Tao et al. (2020).

312

313 2.3.2 Classification of particle type based on hygroscopicity or volatility

314 In this study, ambient aerosol particles were classified into two groups based on their
315 hygroscopicity (hydrophobic and hydrophilic) and two groups based on their volatility (non-volatile
316 and volatile) based on the measurements from H/V-TDMA (Wehner et al., 2009; Liu et al., 2011;
317 Zhang et al., 2016). Each group can be defined using the critical values of GF or SF as follows:
318 hydrophobic population: $\text{GF} < \text{GF}_C$; hydrophilic population: $\text{GF} \geq \text{GF}_C$; non-volatile population: $\text{SF} \geq \text{SF}_C$;
319 and volatile population: $\text{SF} < \text{SF}_C$.

320 The critical values of GF (GF_C) and SF (SF_C) in H/V-TDMA depend on the particle size and
321 working conditions, such as relative humidity and heating temperature. During this campaign, the SF_C

322 was set to 0.85 for all seven measured particle sizes at a temperature of 200 °C. The GF_C for the four
 323 measured particle sizes of 50, 100, 150, and 200 nm were 1.1, 1.15, 1.175, and 1.2, respectively, and
 324 the corresponding hygroscopicity parameter, κ , was approximately 0.07. These values of GF_C and SF_C
 325 divide the probability density functions (PDFs) of SF and GF into two modes as shown in Figure 2c,
 326 consistent with prior NCP studies (Liu et al., 2011; Zhang et al., 2016-), and may be different from
 327 those GF_C and SF_C in other studies because of the difference in aerosol micro-physical properties. The
 328 NF for the hydrophilic group (NF_H) and volatile group (NF_V) can be calculated as follows:

$$329 \quad NF_H = \int_{GF_C}^{\infty} GFPDF(GF)dGF \quad (7)$$

$$330 \quad NF_V = \int_0^{SF_C} SFPDF(SF)dSF \quad (8)$$

331 where GFPDF and SFPDF are the PDFs of GF and SF, respectively, derived from H/V-TDMA
 332 measurements.

333 2.3.3 Classification of particle type based on DMA-SP2 measurements

334 BC-containing aerosolparticles can be categorized into two groups based on coating thickness:
 335 bare BC/thinly coated BC particles and thickly coated BC particles. For the measurement of coated
 336 BC particles at SP2, the incandescence signal is generally detected later than the scattering signals and
 337 the time difference between the occurrence of the peaks of the incandescence and scattering signals is
 338 defined as the lag time (Moteki & Kondo, 2007; Sedlacek et al., 2012; Subramanian et al., 2010). The
 339 coating thickness of BC-containing aerosolparticles in the SP2 measurement can be indicated by the
 340 lag time (Moteki and Kondo, 2007; Schwarz et al., 2006; Sedlacek et al., 2012; Subramanian et al.,
 341 2010; Metcalf et al., 2012), which has exhibited a clear two-mode distribution in previous studies
 342 (Zhang et al., 2018; Zhao et al., 2021). A critical lag time threshold can be used to differentiate between
 343 the different types of BC-containing aerosolparticles and calculate the NF of bare and coated BC
 344 particles in the total identified aerosolparticles. In this study, a two-mode distribution of the lag time
 345 (Δt) was observed, and a critical value of 0.8 μs was used to classify the BC-containing particles into
 346 thinly coated (or bare) BC ($\Delta t < 0.8 \mu s$) and thickly coated BC ($\Delta t \geq 0.8 \mu s$). The definitions of all
 347 abbreviations are listed in Table 1.

348 3 Results and discussions

349 3.1 Campaign overview

350 The time series of the meteorological parameters, aerosol mixing state measurements using
351 different techniques, and mass concentrations of the aerosol chemical ~~compositions~~components are
352 shown in Fig. 1. In detail, the measurements of aerosol mixing states include SPAR at an SS of 0.08%
353 by DMA-CCNC, GF-PDF (PDF of GF) at 200 nm by HTDMA, SF-PDF (PDF of SF) at 200 nm and
354 200 °C by VTDMA, and lag time PDF of 200 nm BC-containing particles by DMA-SP2. The SIA,
355 SOA, POA, and BC mass concentrations are shown in Fig. 1 (b). Three periods with significantly
356 different aerosol pollution conditions were identified during the campaign. As shown in Fig. 1(b),
357 before the 23rd of October (moderately polluted period), the accumulation of aerosols led to SIA mass
358 concentrations $<20 \mu\text{g}/\text{m}^3$. In contrast, the highest mass concentrations of SOA, POA, and BC all
359 reached $10 \mu\text{g}/\text{m}^3$. The mass concentrations of different aerosol components increased significantly
360 from the 23rd of October to the 6th of November (heavily polluted period with an average non-
361 refractory PM_{10} mass concentration of $49.5 \pm 22.5 \mu\text{g}/\text{m}^3$) and decreased ~~to~~to much lower levels after
362 the 6th of November (clean period with a non-refractory PM_{10} mass concentration of $5.1 \pm 3.3 \mu\text{g}/\text{m}^3$).
363 Two particle groups were identified concerning the CCN activity, hygroscopicity, volatility, and
364 coating thickness, as demonstrated by the SPAR, GF-PDF, SF-PDF, and lag-time PDF of BC-
365 containing particles. Significant variations in the aerosol mixing states were also observed during the
366 three periods with different pollution conditions, as demonstrated by the variations in SF-PDF
367 measured by VTDMA. For example, the SF of the non-volatile particle group decreased during the
368 heavily polluted period. Aerosol mixing states may have changed because of various transformations
369 in existing aerosol particles and distinct secondary formation processes under different pollution
370 conditions (Kuang et al., 2020; Tao et al., 2021; Shi et al., 2022; Yang et al., 2022). Diurnal variations
371 in the mass concentrations of different aerosol chemical components and mixing states can be observed
372 in the variations in the SPAR measurements, as previously observed in this region (Liu et al., 2011;
373 Ma et al., 2012; Kuang et al., 2015; Tao et al., 2020).

374 Fig. 2 shows the campaign-averaged SPAR at the three SSs, PDF of the lag time of BC-containing
375 particles, GFPDF, and SFPDF at 200 °C for different particle sizes. The sigmoidal SPAR curves were
376 characterized by a rapid increase, followed by a gradual increase to unit 1, similar to the measured

377 SPAR curves previously observed in this region (Deng et al., 2011; Zhang et al., 2014; Ma et al., 2016;
378 Tao et al., 2018). At lower SSs, the particle size required for CCN activation was larger; thus, rapid
379 increases in the SPAR curves occurred at larger particle sizes as expected. In addition, the maximum
380 AR of the SPAR curves decreases as fewer particles are CCN-active under low SSs. For the three
381 measured SSs, the particle sizes where SPAR equals approximately 0.5 are approximately 90, 120,
382 and 180 nm for the three SSs of 0.08%, 0.14%, and 0.22%, respectively, consistent with the average
383 D_a (see Eq. 7) values of the campaign. The NF of CCN-active particles in large-diameter ranges (which
384 varies with SS and, for example, is greater than 200 nm for 0.08%) can be indicated by the gradual
385 increase in the SPAR curves and quantified by the fitting parameter, MAF (see Eq. 7). The PDFs of
386 the lag time, GF, and SF were all characterized by a bimodal distribution, which indicates two particle
387 groups of BC-containing aerosol particles with different coating thicknesses, hygroscopicity, and
388 volatility. The variations in the aerosol mixing states were further analyzed based on the measured
389 mixing state parameters.

390 3.2 Intercomparisons among aerosol mixing state parameters derived using four techniques

391 The size-dependent characteristics of the aerosol mixing state parameters derived from the
392 measurements of the four techniques and the MFs of different aerosol chemical
393 compositions components during the three pollution periods are shown in Fig. 3. In general, the size-
394 dependent characteristics of MAF, NF_H , NF_V , and NF_{noBC} were similar, suggesting that they were
395 likely dominated by the same particle group, namely BC-free particles. This particle group had the
396 highest number fraction (>0.7) during the heavily polluted period and the lowest number fraction
397 (down to 0.5) during the clean period, with the fraction decreasing with increasing particle size. This
398 suggests that primary emissions tend to have higher number fractions of BC-containing particles in
399 larger diameter ranges; for example, the number fraction of BC-containing particles increases from
400 ~ 0.1 to ~ 0.4 as the particle size increases from 200 to 500 nm during the cleaning clean period. Because
401 the bulk aerosol MF is mostly contributed by particles >300 nm, there may have been more hydrophilic,
402 volatile, CCN-active, and BC-free particles with larger sizes (>300 nm) during the heavily polluted
403 period owing to strong SA formation in larger diameter ranges (Kuang et al., 2020), resulting in a
404 higher NF of these particles compared to the clean period. As for R_{exBC} As for R_{exBC} , which is defined
405 as the number concentration ratio of externally mixed BC particles in total BC-containing particles,

406 the small size dependence of R_{exBC} during the moderately polluted period might have been associated
407 with stronger primary emissions, while the decrease in R_{exBC} with increasing particle diameter in the
408 polluted period confirmed that SA formation is more efficient for particles with larger diameters.

409 As for the difference among the aerosol mixing state parameters, NF_V and NF_{noBC} agreed with
410 each other with a <0.1 difference, and both were higher than NF_H by at least $0.1 NF_H$ in the moderately
411 polluted period. Compared with NF_{noBC} , NF_V was higher during the heavily polluted period, when the
412 nitrate mass fraction was the highest ($\sim 30\%$). The SOA mass fraction was the lowest ($\sim 7\%$) among all
413 three periods, suggesting that some BC-containing aerosolparticles in this period were also identified
414 as volatile, consistent with the fact that the formation of semi-volatile nitrate in BC-containing particles
415 increases their volatility. However, during the cleaningclean period, NF_V was even lower than NF_{noBC} ,
416 suggesting that some BC-free aerosolparticles were characterized as low volatile and non-negligible
417 number fractions of BC-free aerosolparticles dominated these less volatile aerosol components, which
418 were likely less volatile organic aerosols (not likely contributed by BC-containing particles with a BC
419 smaller than the SP2 detection limit, because ~~the SF of~~ this type of volatile BC-containing
420 aerosolparticles has an SF lower than 0.4 (=80 nm/200, nm), which is substantially lower than the
421 threshold SF of 0.85 for NF_V calculation). In addition, the MAF values generally agreed with the NF_H
422 during the clean period. However, they were larger than the NF_H during the moderately and heavily
423 polluted periods (by ~ 0.2) when the POA/SOA mass fractions were higher ($\sim 40\%$ vs. $\sim 35\%$). POA
424 generally has a lower hygroscopicity than SOA. The critical κ of hydrophilic mode aerosols was 0.07,
425 suggesting that a higher number fraction of aerosols had κ below 0.07 (i.e., hydrophobic mode aerosols
426 in this study) during the moderately polluted period. However, under supersaturated conditions, they
427 demonstrate enhanced hygroscopicity by becoming CCN-active. NF_H was consistently lower than NF_V
428 and NF_{noBC} (the average difference between NF_H and NF_{noBC} was approximately 0.2). As mentioned
429 above, NF_H was also lower than MAF during moderately polluted periods, and there may be a
430 significant number fraction of volatile BC-free aerosolparticles with hygroscopicity lower than the
431 critical κ value of 0.07; however, they were still CCN-active and therefore not fully hydrophobic.

432 The diurnal variations in MAF, NF_H , NF_V , and NF_{noBC} , along with the MFs of the aerosol
433 chemical components during the three periods, are shown in Fig. 4. Except for a particle size of 50 nm,
434 the diurnal variations in these four mixing state parameters were generally similar for all measured

435 sizes. The different diurnal variations at a particle size of 50 nm may be due to the different effects of
436 emissions and aging processes on the different aerosol modes, as particles <100 nm mainly reside in
437 the Aitken mode, which is where particles >100 nm mainly reside in the accumulation mode (Wang et
438 al., 2022). For particles >100 nm (Fig. 4 and S5), there was a maximum in the afternoon for MAF,
439 NF_H , NF_V , and NF_{noBC} , indicating a peak during this time due to an increase in SA compositions, such
440 as nitrate and SOA, and a decrease in POA and BC. Diurnal variations in the aerosol mixing state
441 parameters and chemical compositions were more pronounced during the moderately polluted period.
442 During heavily polluted periods, the diurnal variation was least pronounced for NF_V and most
443 pronounced for NF_H . In the clean-air period, there was another maximum at midnight for MAF and
444 NF_{noBC} , which may be attributed to the diurnal variations in SA compositions, such as sulfate and SOA,
445 and the decrease in BC and FFOA. The average-size dependence of the aerosol mixing state parameters
446 over different time ranges during a heavily polluted period is shown in Fig. S6. It can be seen that the
447 differences among the four parameters were the least from 12:00 to 18:00, with the most SOA and the
448 least POA. This is consistent with the results shown in Fig. 3, where the difference between the MAF
449 and NF_H decreased when the POA mass fractions were the smallest. R_{exBC} tended to be lower during
450 the daytime, and its diurnal variation was more significant for larger particle sizes. In general, the
451 diurnal variations for R_{exBC} were opposite to those of NF_{noBC} and agreed better with those of the
452 primary aerosol MFs. This is because BC particles originate from primary emissions and are mainly
453 mixed externally. After aging in the atmosphere, BC particles can be coated by SAs, resulting in more
454 coated BC particles and fewer externally mixed BC particles. As SAs tend to form on larger particles,
455 the diurnal variations in SA formation may significantly affect the R_{exBC} of larger particle sizes.

456 As summarized in Table. S1, the comparison among MAF, NF_H , NF_V , and NF_{noBC} was
457 conducted based on their correlations with different particle sizes. Note that the MAF at SSs of 0.08%,
458 0.14%, and 0.22% were used for comparison at 200, 150, and 100 nm particle sizes. This is because
459 the diameter range of rapid increases in the SPAR curves is determined by aerosol hygroscopicity in
460 this particle size range. The midpoints of the rapidly increasing diameter ranges of the SPAR curves
461 at SSs of 0.08%, 0.14%, and 0.22% were approximately 180 nm, 120 nm, and 90 nm, respectively (as
462 shown in Fig. 2). In general, there were moderate correlations ($r \sim 0.5$) between MAF, NF_H , and NF_V ,
463 suggesting that a similar particle group contributed to the dominance of CCN-active, hygroscopic, and

464 volatile aerosols (Zhang et al., 2016). The agreement between MAF and NF_V was slightly higher than
465 that between MAF and NF_H or between NF_H and NF_V ~~with. In detail, compared to the other two, the~~
466 ~~agreement between MAF and NF_V has a~~ similar correlation coefficients ~~($r \sim 0.65$). However,) and a~~
467 smaller systematic differences (slope and intercept) were much closer to 1 and 0, respectively. This
468 is consistent with the previous finding that a substantial number fraction of volatile but less
469 hygroscopic aerosols are CCN-active. For smaller particle sizes, the correlation became weaker
470 ($r \sim 0.4$), whereas the degree of reduction was the lowest for the correlation between MAF and NF_V :
471 ($r \sim 0.529$).

472 3.3 Impacts of primary aerosol emissions on aerosol mixing states and parameter 473 intercomparisons

474 Fig. 5 presents the correlation between each aerosol mixing state parameter at 200 nm and the
475 MF of each primary organic aerosol composition during the three periods. The four mixing state
476 parameters (MAF, NF_H , NF_V , and NF_{noBC}) were negatively correlated with MF_{FFOA} and MF_{BBOA} .
477 However, the anticorrelation with MF_{FFOA} ($-0.45 \sim -0.74$) was much stronger than MF_{BBOA} ($-0.10 \sim$
478 0.45). Biomass-burning emissions and fossil fuel emissions are the two major sources of BC in the
479 NCP (Yang et al., 2022), and NF_{noBC} was negatively correlated with MF_{FFOA} ($r = -0.49$) and weakly
480 correlated ($r = -0.18$) with MF_{BBOA} , suggesting that fossil fuel emissions were likely the dominant
481 source of BC during this field campaign. The negative correlation between MAF and MF_{FFOA} was
482 weaker than that of NF_{noBC} with MF_{FFOA} (-0.62 vs. -0.49). In particular, at the same MF_{FFOA} , the MAF
483 was lower than NF_{noBC} , demonstrating that some BC-free particles were CCN-inactive and were likely
484 mainly composed of organic aerosols from fossil fuel combustion emissions. The negative correlation
485 between NF_V and MF_{FFOA} was slightly weaker than between NF_{noBC} and MF_{FFOA} (-0.56 vs. -0.49). At
486 the same MF_{FFOA} , NF_{noBC} was close to NF_V , and considering that BC-containing aerosol particles were
487 dominated by thinly coated BC most of the time (Fig. 5), this demonstrates that the non-volatile
488 population identified by V-TDMA was mainly contributed by BC-containing aerosol particles. NF_H
489 had the lowest negative correlation with MF_{FFOA} ($r = -0.74$), demonstrating significant contributions
490 from fossil fuel emissions to nearly hydrophobic aerosol populations. At the same MF_{FFOA} , ~~NF_H was~~
491 ~~obviously lower than NF_{noBC} (NF_H and NF_{noBC} were larger and smaller than 0.7 for example, when~~
492 ~~conditions of MF_{FFOA} was larger than ≥ 0.1), demonstrating were met, NF_H (< 0.7) demonstrated a~~

493 noticeable decrease compared to NF_{noBC} (>0.7), and NF_H showed a negative correlation with both
494 MF_{BBOA} and MF_{FFOA} , suggesting that a substantial portion of nearly hydrophobic aerosols ~~was not~~
495 ~~contributed by BC-containing aerosols (BC-containing aerosols of 200 nm with BC core smaller than~~
496 ~~80 nm which is smaller than the detection limit of SP2 likely to be quite aged in the air, thus not~~
497 ~~possible to be nearly hydrophobic), but likely by particles originated from~~ FFOA- or BBOA-dominant
498 ~~aerosols (NF_H also had a negative correlation with MF_{BBOA}). However, therather than BC-containing~~
499 ~~particles. Additionally,~~ markedly different correlations were observed between MAF and MF_{FFOA} ($r=-$
500 0.62), and between MAF and MF_{BBOA} ($r=-0.2$) ~~imply~~, implying that nearly hydrophobic but CCN-
501 active aerosols ~~were~~ likely contributed by/originated from biomass- ~~burning-emissions~~. The
502 correlations between the ratio of thinly coated BC in the total BC-containing particles (R_{exBC}) and the
503 MFs of BBOA and FFOA are shown in Fig. 6. Weak correlations ($r<0.3$) between R_{exBC} and MF_{BBOA}
504 and MF_{FFOA} were observed. However, R_{exBC} tended to increase with MF_{FFOA} , suggesting that BC-
505 containing aerosolsparticles emitted from fossil fuel combustion tended to be more externally mixed
506 with other aerosol components than those emitted from biomass burning-, which is consistent with the
507 results of previous studies (Schwarz et al., 2008; Laborde et al., 2013; Liu et al., 2017; Zhang et al.,
508 2020). These results demonstrate remarkably different mixing states and the physical and chemical
509 properties of fossil fuel combustion and biomass-burning aerosols.

510 The impact of primary emissions on the differences among the four aerosol mixing state
511 parameters at a particle size of 200 nm was analyzed and is shown in Fig. 7. The difference between
512 NF_{noBC} and NF_H ($NF_{noBC}-NF_H$) was significantly positively correlated with MF_{FFOA} and MF_{BBOA}
513 ($r>0.5$), suggesting that a substantial proportion of POA resided in BC-free aerosolsparticles and was
514 volatile, but contributed substantially to nearly hydrophobic aerosols; as did the differences between
515 NF_V and NF_H (NF_V-NF_H). The MFs of BBOA and FFOA were poorly correlated with the differences
516 between the MAF and NF_V ($MAF-NF_V$), MAF and NF_{noBC} ($MAF-NF_{noBC}$), and NF_V and NF_{noBC} (NF_V-
517 NF_{noBC}) (Fig. S7). The difference between MAF- and NF_H was positively correlated with MF_{BBOA} ,
518 further suggesting that BBOA contributed to nearly hydrophobic aerosols under subsaturated
519 conditions; however, their hygroscopicity was enhanced, and they became CCN-active under
520 supersaturated conditions. The enhanced hygroscopicity of BBOA under supersaturated conditions
521 may be attributed to: (1) surface tension lowered by surface-active organic solutes (Hodas et al., 2016;

522 Ruehl et al., 2016); (2) liquid–liquid phase separation (Ovadnevaite et al., 2017; Liu et al., 2018); (3)
523 dissolution of sparingly soluble compounds at higher saturated conditions (Wex et al., 2009; Dusek et
524 al., 2011); (4) highly viscous organic aerosol which takes up water by surface water adsorption under
525 sub-saturated conditions and by absorption of water under super-saturated conditions (Pajunoja et al.,
526 2015). The correlations between the mixing-state parameters and primary aerosol composition during
527 the campaign and different pollution periods are summarized in Fig. S7.

528
529 In general, both field and laboratory studies have shown that primary organic aerosols from the
530 combustion of biomass and fossil fuels are less hygroscopic. In laboratory experiment, it is found
531 that organic aerosols produced by fossil fuels have very low hygroscopicity, significantly less than
532 0.1 (Vu et al., 2015, 2017; Fofie et al., 2018; Zhang et al., 2018; Mukherjee et al., 2021).
533 Observations have also found that the organic aerosols associated with fossil fuel combustion have
534 low hygroscopicity, which may be due to the low soluble components in FFOA (Qiu et al., 2019; Li
535 et al., 2021). The aerosol composition produced by biomass burning is complex, with a large number
536 of organic aerosols (BBOA) and inorganic components being produced at the initial stage, making
537 important contributions to CCN (Spracklen et al., 2011; Bougiatioti et al., 2016; Pöhlker et al.,
538 2018). These primary organic aerosols (i.e. BBOA) is generally semi-volatile (May et al. 2013) and
539 less hygroscopic (Engelhart et al., 2012; Hennigan et al., 2012), which has a negative contribution to
540 overall hygroscopicity (Bougiatioti et al., 2016; Kuang et al., 2020b, 2021, Cai et al., 2022), resulting
541 in weaker overall aerosol hygroscopicity in the initial stage of the biomass burning (Engelhart et al.,
542 2012, Hennigan et al., 2012, Pöhlker et al., 2018). However, laboratory experiments found that
543 BBOA may contain organic substances with different hygroscopicity under different saturation ratios
544 (Malek et al., 2022), lead to increased hygroscopicity and enhanced CCN activity of BBOA under
545 supersaturation conditions (Hersey et al., 2013). Our results generally agree with previous studies
546 and provide evidences of the enhanced CCN activity of BBOA under supersaturation conditions in
547 field campaigns. Furthermore, the different impacts of aerosols emitted from biomass burning and
548 fossil fuel combustion on CCN is directly observed in this campaign used newly developed advanced
549 aerosol-cloud sampling system, which show that biomass burning aerosols are efficient CCN even
550 under low supersaturations (<0.05%), however, aerosols from fossil fuel combustions can only

551 activate at higher supersaturations ($\sim 0.14\%$). These results suggest simultaneous measurements of
552 aerosol GF distributions, SPAR curves and BC mixing states and their comparisons could shed novel
553 insights into different synergistic hygroscopic, volatile and activation properties of aerosols from
554 different sources in the atmosphere.

555 3.4 Impacts of SA formation on aerosol mixing states and parameter intercomparisons

556 The correlations between the aerosol mixing state parameters at 200 nm and the MF of each SA
557 component are presented in Fig. 8 for three periods, and the entire campaign is presented. The analysis
558 is conducted at only 200 nm, where all four aerosol mixing state parameters were measured to compare
559 the four aerosol mixing state parameters and their relationships with aerosol chemical
560 compositions components simultaneously. Generally, MAF, NF_H , NF_V , and NF_{noBC} exhibited strong
561 positive correlations with MF_{NH_4} ($r > 0.5$). This is likely because ammonium was mainly formed
562 through neutralizing sulfuric and nitric acids with ammonia; therefore, variations in ammonium better
563 represent overall secondary inorganic aerosol formation. As shown in Fig. 3, the secondary inorganic
564 aerosol components dominated over SA (approximately 50% vs. SA (the mass ratio between SIA and
565 SA is approximately 70%), indicating that SA formation was primarily composed of secondary
566 inorganic aerosol formation, which explains the weaker correlation with SOA ($r \sim 0.3$), as shown in
567 Fig. 8.

568 During the clean-air period, when the MFs of SOA and sulfate were both above 15%, all four
569 parameters had a strong positive correlation with MF_{SO_4} and MF_{SOA} ($r > 0.5$), suggesting that when a
570 clean background air mass with higher mass fractions of sulfate and SOA prevailed, the local primary
571 emissions that contributed substantially to BC-containing and less hygroscopic POA aerosols became
572 less significant. The positive correlations between the MAF and SA components have been extensively
573 discussed by Tao et al. (2021), who found that SA formation enhances the hygroscopicity of nearly
574 hydrophobic aerosols, thereby increasing CCN activity. This also explains the strong correlation
575 between the NF_H or MAF and ammonium formation. The strong positive correlations between NF_V
576 and SA formation ($r \sim 0.6$) are consistent with the fact that nitrate dominates SA formation during this
577 campaign and is semi-volatile. For the first time, strong positive correlations between NF_{noBC} and SA
578 formation were observed ($r = 0.6$). NF_{noBC} depends primarily on the relative variation between BC-
579 containing and BC-free aerosol particles. The increase in NF_{noBC} at 200 nm as a function of the SA

580 MF suggests that SAs migrated to a higher mass fraction of BC-free aerosol particles smaller than 200
581 nm to particle size of 200 nm, highlightingsuggesting that SAs tended to form more quickly on BC-
582 free aerosol particles than on BC-containing aerosols- particles with BC higher than SP2 detection
583 limit. Recent studies reported that catalyst or photochemical reactions on BC particles can contribute
584 the formation of secondary aerosols (Zhang et al., 2020; Zhang et al., 2021). Our results may indicate
585 SA formation on BC particles might not be a significant pathway that contribute substantially to haze
586 formation, and the underlying mechanisms need to be further resolved.

587 The effects of SA formation on the differences between the four aerosol mixing state parameters
588 were studied and are illustrated in Fig. 9. The two OOA factors (OOA1 and OOA2) were formed
589 through different chemical pathways. The difference between NF_{noBC} and NF_H ($NF_{noBC}-NF_H$) showed
590 a strong negative correlation with MF_{NH_4} and MF_{NO_3} (mainly -0.6), as did the differences between NF_V
591 and NF_H (NF_V-NF_H). ~~As previously noted, NF_H typically has smaller values than NF_V and NF_{noBC} .~~
592 ~~Thus, a negative correlation between the MFs of ammonium and Ammonium nitrate indicated that the~~
593 ~~formation of secondary nitrate resulted in a smaller difference between these mixing state parameters.~~
594 ~~An increase in the fraction of ammonium nitrate, is~~ a pure-scattering semi-volatile compound with
595 strong hygroscopicity, the increase of its mass fraction can ~~render the~~enhance both aerosol population
596 more dominated by particles with strong volatility and hygroscopicity. ~~As the secondary inorganic~~
597 ~~aerosol components increase, this can result, therefore resulting~~ in a smaller difference between NF_{noBC} ,
598 NF_H , and NF_V .

599 Furthermore, the difference between NF_V and NF_H showed a positive correlation with MF_{OOA2}
600 and a negative correlation with MF_{OOA1} , indicating different volatility and hygroscopicity of the two
601 SOA factors. The differences between NF_V and NF_H concerning the MF of OOA1 and OOA2 are
602 shown in Fig. 9(e) and (f), respectively. As previously noted, NF_V was generally higher than NF_H , and
603 the difference between the two decreased with increasing MF_{OOA1} , which was generally smaller than
604 0.3. This suggests that the formation of OOA1 enhances the hygroscopicity of volatile particles, which
605 aligns with the highest oxidation state of OOA1 (higher O/C but lower H/C compared to OOA2) and
606 has a significant and overall positive impact on aerosol hygroscopicity (Cerully et al., 2015; Thalman
607 et al., 2017; Zhang et al., 2023). A positive correlation was observed between NF_V and MF_{OOA2}
608 ($r \sim 0.25$).

609 In contrast, the correlation between NF_H and MF_{OOA2} was weak (R was close to 0), implying that
610 OOA2 might be semi-volatile but only weakly hygroscopic, which could contribute to NF_V being
611 higher than NF_H as OOA1 increases. The difference between NF_{noBC} and NF_V ($NF_{noBC}-NF_V$) was
612 negatively correlated with MF_{NO3} , which is consistent with the semi-volatile nature of nitrate. The
613 negative correlation between $NF_{noBC}-NF_V$ and MF_{OOA2} indicates that the difference is smaller when
614 there is more OOA2, implying that OOA2 is also a semi-volatile compound and is likely formed
615 mainly on BC-free particles: (particles with BC mass lower than detection limit are not excluded). The
616 correlations between the differences between NF_V-MAF and $NF_{noBC}-MAF$ and the MF of each SA
617 composition were very weak. The impacts of SA formation on BC mixing states are shown in Fig. S8.
618 In general, the NF of thinly coated BC has a negative correlation with SIA and a weak association with
619 SOA, suggesting that SIA formation mainly enhances the thickness of the BC coating. The correlations
620 between the mixing state parameters and SA composition during the campaign and different pollution
621 periods are summarized in Fig. S9. Our results on OOA agree with previous studies, that OOA are
622 reported to be volatile (Kim et al., 2020; Cai et al., 2022) but can have a positive or negative impact
623 on hygroscopicity depending on its oxidation level (Kim et al., 2020; Kuang et al., 2021; Cai et al.,
624 2022).

625 In addition to changes in the MFs of SA compositions, the accumulation of SA pollution may
626 provide insights into the impact of SA formation on aerosol mixing states. As shown in Fig. 10(a),
627 during the heavily polluted periods, there were two distinct pollution accumulation processes from the
628 23rd to the 27th of October and from the 28th to the 31st of October, respectively. During the pollution
629 accumulation process, the mass concentration of SAs increased by approximately three-fold, indicating
630 the rapid formation of secondary compositions and a significant increase in non-refractory PM_{10} (NR-
631 PM_{10}) mass concentration. Fig. 10(b) and (c) illustrate that this increase in SAs significantly
632 enhanced/enlarged the value of aerosol mixing state parameters, including MAF, NF_V , NF_H , and NF_{noBC} ,
633 which increased from approximately 0.5 to 0.8 with evident diurnal variations. This highlights the
634 impact of SA formation on the aerosol mixing states and the importance of studying the pollution
635 accumulation processes of SAs. The enhancements in the different aerosol mixing state parameters
636 during the pollution accumulation process were not uniform. MAF and NF_H initially exhibited lower
637 values than NF_V and NF_{noBC} ; however, their later enhancement was stronger than that of NF_{noBC} . Fig.

638 10(d) and (e) show the difference between NF_{noBC} and NF_V at 200 and 300 nm as a function of SA
639 mass concentrations during these two pollution periods, which clearly shows how, during SA
640 formation, NF_V became higher than NF_{noBC} while NF_V remained close to the NF of thickly coated BC-
641 containing aerosolparticles (NF_{CBC}) plus NF_{noBC} ($NF_{CBC}+NF_{CBC}$). These results suggest that SA
642 formation increases the volatility of BC-free and BC-containing aerosolparticles, leading to an
643 increased NF_V compared with NF_{noBC} . Almost all BC-free particles and some BC-containing
644 aerosolparticles become volatile during the accumulation of pollution.

645

646 4. Conclusions

647 The aerosol mixing state is one of the most important physicochemical properties of aerosol
648 particles and significantly affects their optical properties and the CCN activity of aerosol particles. The
649 aerosol mixing states vary significantly with complex aerosol emissions and atmospheric
650 transformations. In this study, aerosol mixing states derived from CCN activity, hygroscopicity,
651 volatility, and BC particle observations, along with their relationship to primary aerosol emissions and
652 SA formation, were systematically analyzed based on simultaneous measurements of CCNC,
653 H/VTDMA, and SP2. Statistical analysis demonstrated that the NFs of CCN-active, hygroscopic, and
654 volatile particles were generally positively correlated and mainly contributed by BC-free
655 aerosolparticles. Therefore, four mixing state parameters -were all negatively correlated to either the
656 MFs of BBOA or FFOA because fossil fuel combustion and biomass burning were the two major
657 sources of BC-containing aerosolparticles during this field campaign. However, the differences
658 between these mixing state parameters varyvaried significantly under different conditions, have shed
659 new insights into aerosol physical and chemical properties and even secondary aerosol formation
660 mechanisms.

661 ~~The intercomparison results highlight the differences in the aerosol mixing states and~~
662 ~~physicochemical properties caused by fossil fuel combustion and biomass burning emissions. The~~
663 ~~CCN and SP2 measurements showed that CCN-inactive BC-free particles were mainly produced by~~
664 ~~fossil fuel combustion. In contrast, a comparison between the VTDMA and SP2 measurements~~
665 ~~indicated that the non-volatile aerosols mostly comprised BC-containing particles. The comparison~~
666 ~~between HTDMA and SP2 measurements revealed that a significant proportion of nearly hydrophobic~~

667 aerosols was not from BC-containing particles but from fossil fuel combustion or biomass-burning-
668 dominated organic aerosols. The correlation between the CCNC and HTDMA measurements also
669 showed that nearly hydrophobic, BC-free aerosols could become CCN-active under supersaturated
670 conditions and are tightly linked to biomass-burning emissions. This suggests that biomass-burning
671 aerosols may exhibit different hygroscopicities under sub- and supersaturated conditions (Bougiatioti
672 et al., 2016). Furthermore, the correlation analysis between SP2 measurements and the MFs of BBOA
673 and FFOA indicated that BC-containing aerosols from fossil fuel combustion tended to be more
674 externally mixed with other aerosol compositions than those from biomass-burning activities.

675 In addition to primary aerosol emissions, SA formation also significantly impacts variations in
676 aerosol mixing states. During this campaign, SA formation was dominated by nitrate and SOA
677 production, which had markedly different impacts on the aerosol mixing states owing to their different
678 physical properties and formation pathways. NF_{noBC} , MAF, NF_H , and NF_V were all positively
679 correlated with the nitrate and SOA MFs, revealing much stronger correlations with SOA than nitrate.
680 This is consistent with the semi-volatile but highly hygroscopic properties of nitrates. The high
681 correlation coefficient between NF_{noBC} and the MFs of SAs at 200 and 300 nm suggests that SA
682 formation led to the migration of BC-free aerosols towards larger diameters more quickly than that of
683 BC-containing aerosols. This result reveals that SAs formed more rapidly on BC-free than on BC-
684 containing aerosols, which aligns with the hydrophobic nature of BC-containing aerosols that do not
685 favor aqueous SA formation. Moreover, as the MFs of nitrate or ammonium increased, the differences
686 between the mixing state parameters (NF_{noBC} , MAF, NF_H , and NF_V) decreased because of the
687 hygroscopic and semi-volatile nature of ammonium nitrate. However Fossil fuel combustion and
688 biomass burning emissions represent two major primary sources of global aerosol burden and are
689 dominant primary aerosol sources in this campaign. It is known that the chemical compositions of both
690 these primary sources are dominated by organics and BC. However, the intercomparison results among
691 instruments revealed significant differences in the physical and chemical properties of aerosols emitted
692 from these two sources. The combination of HTDMA, DMA-SP2, as well as aerosol source
693 apportionment confirmed that substantial portions of BC-free aerosols from both biomass burning and
694 fossil fuel combustion are nearly hydrophobic under sub-saturated conditions. Additionally, BC from
695 fossil fuel combustion tends to be more externally mixed with other aerosol compositions than those

696 from biomass burning. However, additional insights from DMA-CCN measurements revealed that
697 substantial portions of BC-free aerosols, nearly hydrophobic from biomass burning, could serve as
698 CCN, while a substantial portion of those from fossil fuel combustion could not. Previous studies have
699 confirmed the hygroscopicity difference of aerosols from biomass burning under sub- and
700 supersaturated conditions in laboratory settings; however, such differences have rarely been confirmed
701 in field measurements. Moreover, comparisons between sub- and supersaturated conditions for
702 aerosols from fossil fuel combustion have been rarely undertaken, even in laboratory studies. This
703 finding is quite important because the ability of primary organic aerosols from biomass burning and
704 fossil fuel combustion is often treated as the same in models (Liu et al., 2021; Pöhlker et al., 2023).

705 Secondary aerosol formation substantially alters aerosol mixing state. The different variations in
706 mixing state parameters can also help reveal mechanisms of secondary aerosol formation. For example,
707 the two resolved SOA factors exhibited different impacts on the differences between NF_V and NF_H
708 ($NF_V - NF_H$), and their correlations with NF_V and NF_H revealed that OOA_I was more hygroscopic but
709 less volatile, suggesting distinct formation mechanisms for these two OOA factors—~~during the field~~
710 ~~campaign.~~— Further analysis might help link SOA formation mechanisms to aerosol physical
711 properties, which is important for connecting aerosol chemistry to aerosol climate effects determined
712 by aerosol physicochemical properties. Additionally, variations in size-resolved NF_{noBC} revealed that
713 secondary organic and inorganic aerosol formations led to the migration of BC-free particles towards
714 larger diameters more quickly than that of BC-containing particles. This phenomenon is more likely
715 to occur when aqueous pathways dominate secondary aerosol formation because BC-containing
716 particles generally exhibit weak hygroscopicity and do not favor aqueous processes.

717 The findings of this study highlight the markedly different effects of primary emissions and SA
718 formation on aerosol mixing states and suggest that comparisons of aerosol mixing states obtained
719 using various techniques are useful for gaining insights into the hygroscopicity, volatility, and CCN
720 activity of different aerosols. ~~These comparisons also indicate~~ Recommendations are listed for future
721 studies based on the findings of this study: (1) When exploring the impact of SA aerosol emissions and
722 secondary aerosol formations on aerosol hygroscopic under sub- and supersaturated conditions, we
723 recommend employing simultaneous DMA-SP2 measurements to better represent BC characteristics;
724 (2) Simultaneous DMA-CCNC, V-HTDMA, and DMA-SP2 measurements could enhance studies on

725 secondary aerosol formation mechanisms. Conversely, if formation mechanisms and pathways are
726 clear, these measurements could elucidate how secondary aerosol formation impacts aerosol physical
727 properties, which can help understand the pathways of SA formation. However, it is important to from
728 different aspects. (3) To be cautious in the application of aerosol mixing state parameters from HV-
729 TDMA to conduct aerosol optical property investigations because the suitability of ~~VTDMA~~HV-
730 TDMA-derived mixing state parameters for representing BC mixing states is largely dependent on the
731 composition and mass of the ~~SAs~~-secondary aerosols, and DMA-SP2 measurements are recommended
732 for this purpose.

733

734 **Data availability.** The data used in this study are available from the corresponding author upon request
735 Ye Kuang (kuangye@jnu.edu.cn) and Li Liu (liul@gd121.cn)

736 **Competing interests.** The authors declare that they have no conflict of interest.

737

738 **Author Contributions.**

739 YK and WY planned this campaign and YK designed the aerosol experiments and conceived this
740 research together with JC, and JC wrote the manuscript. JC performed measurements of CCNC, BL
741 performed measurements of SP2 and analyzed SP2 datasets with the help of GZ, WQ and YL
742 performed AMS measurements, LL performed HV-TDMA measurements and conducted post-data
743 processing as well as some of data analysis. BX, HX, MMZ, HZ and SR participated this campaign
744 and helped instruments maintenance. GZ provided full support for the campaign. All authors
745 contributed to discussions and revisions of this paper.

746 **Financial supports.** This work is supported by National Natural Science Foundation of China
747 (42175083, 42175127, 42275066), the Guangzhou Science and Information Technology Bureau
748 Project (2023A04J0941), the Guangdong Provincial Key Research and Development Program (grant
749 no. 2020B1111360003), the Science and Technology Innovation Team Plan of Guangdong
750 Meteorological Bureau (grant no. GRMCTD202003).

751

752 **References**

753 Adachi, K., Sedlacek, A. J., Kleinman, L., Chand, D., Hubbe, J. M., and Buseck, P. R.: Volume
754 changes upon heating of aerosol particles from biomass burning using transmission electron
755 microscopy, *Aerosol Science and Technology*, 52, 46–56,
756 <https://doi.org/10.1080/02786826.2017.1373181>, 2018.

757 Adachi, K., Sedlacek, A. J., Kleinman, L., Springston, S. R., Wang, J., Chand, D., Hubbe, J. M.,
758 Shilling, J. E., Onasch, T. B., Kinase, T., Sakata, K., Takahashi, Y., and Buseck, P. R.: Spherical tarball
759 particles form through rapid chemical and physical changes of organic matter in biomass-burning
760 smoke, *Proceedings of the National Academy of Sciences*, 116, 19336–19341,
761 <https://doi.org/10.1073/pnas.1900129116>, 2019.

762 Bond, T. C., Doherty, S. J., Fahey, D. W., Forster, P. M., Berntsen, T., DeAngelo, B. J., Flanner,
763 M. G., Ghan, S., Kaercher, B., Koch, D., Kinne, S., Kondo, Y., Quinn, P. K., Sarofim, M. C., Schultz,
764 M. G., Schulz, M., Venkataraman, C., Zhang, H., Zhang, S., Bellouin, N., Guttikunda, S. K., Hopke,
765 P. K., Jacobson, M. Z., Kaiser, J. W., Klimont, Z., Lohmann, U., Schwarz, J. P., Shindell, D.,
766 Storelvmo, T., Warren, S. G., and Zender, C. S.: Bounding the role of black carbon in the climate
767 system: A scientific assessment, *Journal of Geophysical Research-Atmospheres*, 118, 5380–5552,
768 <https://doi.org/10.1002/jgrd.50171>, 2013.

769 Bougiatioti, A., Bezantakos, S., Stavroulas, I., Kalivitis, N., Kokkalis, P., Biskos, G.,
770 Mihalopoulos, N., Papayannis, A., and Nenes, A.: Biomass-burning impact on CCN number,
771 hygroscopicity and cloud formation during summertime in the eastern Mediterranean, *Atmos. Chem.*
772 *Phys.*, 16, 7389–7409, <https://doi.org/10.5194/acp-16-7389-2016>, 2016.

773 Cai, M., Tan, H., Chan, C. K., Mochida, M., Hatakeyama, S., Kondo, Y., Schurman, M. I., Xu,
774 H., Li, F., Shimada, K., Li, L., Deng, Y., Yai, H., Matsuki, A., Qin, Y., and Zhao, J.: Comparison of
775 Aerosol Hygroscopicity, Volatility, and Chemical Composition between a Suburban Site in the Pearl
776 River Delta Region and a Marine Site in Okinawa, *Aerosol and Air Quality Research*, 17, 3194–3208,
777 <https://doi.org/10.4209/aaqr.2017.01.0020>, 2017.

778 [Cai, M., Huang, S., Liang, B., Sun, Q., Liu, L., Yuan, B., Shao, M., Hu, W., Chen, W., Song, Q.,](#)
779 [Li, W., Peng, Y., Wang, Z., Chen, D., Tan, H., Xu, H., Li, F., Deng, X., Deng, T., Sun, J., and Zhao,](#)
780 [J.: Measurement report: Distinct size dependence and diurnal variation in organic aerosol](#)
781 [hygroscopicity, volatility, and cloud condensation nuclei activity at a rural site in the Pearl River Delta](#)
782 [\(PRD\) region, China, *Atmos. Chem. Phys.*, 22, 8117–8136, <https://doi.org/10.5194/acp-22-8117-2022>,](#)
783 [2022.](#)

784 Canagaratna, M. R., Jimenez, J. L., Kroll, J. H., Chen, Q., Kessler, S. H., Massoli, P., Hildebrandt
785 Ruiz, L., Fortner, E., Williams, L. R., Wilson, K. R., Surratt, J. D., Donahue, N. M., Jayne, J. T., and
786 Worsnop, D. R.: Elemental ratio measurements of organic compounds using aerosol mass
787 spectrometry: characterization, improved calibration, and implications, *Atmos. Chem. Phys.*, 15, 253–
788 272, <https://doi.org/10.5194/acp-15-253-2015>, 2015.

789 Cerully, K. M., Bougiatioti, A., Hite Jr., J. R., Guo, H., Xu, L., Ng, N. L., Weber, R., and Nenes,
790 A.: On the link between hygroscopicity, volatility, and oxidation state of ambient and water-soluble
791 aerosols in the southeastern United States, *Atmos. Chem. Phys.*, 15, 8679–8694,
792 <https://doi.org/10.5194/acp-15-8679-2015>, 2015.

793 Chen, C., Qiu, Y., Xu, W., He, Y., Li, Z., Sun, J., Ma, N., Xu, W., Pan, X., Fu, P., Wang, Z., and
794 Sun, Y.: Primary Emissions and Secondary Aerosol Processing During Wintertime in Rural Area of
795 North China Plain, *Journal of Geophysical Research: Atmospheres*, 127, e2021JD035430,
796 <https://doi.org/10.1029/2021JD035430>, 2022.

797 Chen, J., Budisulistiorini, S. H., Miyakawa, T., Komazaki, Y., and Kuwata, M.: Secondary
798 aerosol formation promotes water uptake by organic-rich wildfire haze particles in equatorial Asia,
799 *Atmos. Chem. Phys.*, 18, 7781–7798, <https://doi.org/10.5194/acp-18-7781-2018>, 2018.

800 Cheng, Y. F., Su, H., Rose, D., Gunthe, S. S., Berghof, M., Wehner, B., Achtert, P., Nowak, A.,
801 Takegawa, N., Kondo, Y., Shiraiwa, M., Gong, Y. G., Shao, M., Hu, M., Zhu, T., Zhang, Y. H.,
802 Carmichael, G. R., Wiedensohler, A., Andreae, M. O., and Pöschl, U.: Size-resolved measurement of
803 the mixing state of soot in the megacity Beijing, China: diurnal cycle, aging and parameterization,
804 *Atmos. Chem. Phys.*, 12, 4477–4491, <https://doi.org/10.5194/acp-12-4477-2012>, 2012.

805 Ching, J., Fast, J., West, M., and Riemer, N.: Metrics to quantify the importance of mixing state
806 for CCN activity, *Atmos. Chem. Phys.*, 17, 7445–7458, <https://doi.org/10.5194/acp-17-7445-2017>,
807 2017.

808 Ching, J., Adachi, K., Zaizen, Y., Igarashi, Y., and Kajino, M.: Aerosol mixing state revealed by
809 transmission electron microscopy pertaining to cloud formation and human airway deposition, *npj*
810 *Climate and Atmospheric Science*, 2, 22, <https://doi.org/10.1038/s41612-019-0081-9>, 2019.

811 Deng, Z. Z., Zhao, C. S., Ma, N., Liu, P. F., Ran, L., Xu, W. Y., Chen, J., Liang, Z., Liang, S.,
812 Huang, M. Y., Ma, X. C., Zhang, Q., Quan, J. N., Yan, P., Henning, S., Mildenerger, K., Sommerhage,
813 E., Schäfer, M., Stratmann, F., and Wiedensohler, A.: Size-resolved and bulk activation properties of
814 aerosols in the North China Plain, *Atmos. Chem. Phys.*, 11, 3835–3846, [https://doi.org/10.5194/acp-](https://doi.org/10.5194/acp-11-3835-2011)
815 11-3835-2011, 2011.

816 Deng, Z. Z., Zhao, C. S., Ma, N., Ran, L., Zhou, G. Q., Lu, D. R., and Zhou, X. J.: An examination
817 of parameterizations for the CCN number concentration based on in situ measurements of aerosol
818 activation properties in the North China Plain, *Atmos. Chem. Phys.*, 13, 6227–6237,
819 <https://doi.org/10.5194/acp-13-6227-2013>, 2013.

820 [Dusek, U., Frank, G.P., et al., 2011. Water uptake by biomass burning aerosol at sub- and](#)
821 [supersaturated conditions: closure studies and implications for the role of organics. *Atmos. Chem.*](#)
822 [Phys. 11 \(18\), 9519–9532.](#)

823 Drinovec, L., Močnik, G., Zotter, P., Prévôt, A. S. H., Ruckstuhl, C., Coz, E., Rupakheti, M.,
824 Sciare, J., Müller, T., Wiedensohler, A., and Hansen, A. D. A.: The “dual-spot” Aethalometer: an
825 improved measurement of aerosol black carbon with real-time loading compensation, *Atmos. Meas.*
826 *Tech.*, 8, 1965–1979, <https://doi.org/10.5194/amt-8-1965-2015>, 2015.

827 [Engelhart, G. J., Hennigan, C. J., Miracolo, M. A., Robinson, A. L., and Pandis, S. N.: Cloud](#)
828 [condensation nuclei activity of fresh primary and aged biomass burning aerosol, *Atmos. Chem. Phys.*,](#)
829 [12, 7285–7293, https://doi.org/10.5194/acp-12-7285-2012, 2012.](#)

830 Ervens, B.: Modeling the Processing of Aerosol and Trace Gases in Clouds and Fogs, *Chemical*
831 *Reviews*, 115, 4157–4198, <https://doi.org/10.1021/cr5005887>, 2015.

832 Farmer, D. K., Cappa, C. D., and Kreidenweis, S. M.: Atmospheric Processes and Their
833 Controlling Influence on Cloud Condensation Nuclei Activity, *Chemical Reviews*, 115, 4199–4217,
834 <https://doi.org/10.1021/cr5006292>, 2015.

835 Fierce, L., Riemer, N., and Bond, T. C.: Toward Reduced Representation of Mixing State for
836 Simulating Aerosol Effects on Climate, *Bulletin of the American Meteorological Society*, 98, 971–
837 980, <https://doi.org/10.1175/BAMS-D-16-0028.1>, 2017.

838 [Fofie, E. A., Donahue, N. M., and Asa-Awuku, A.: Cloud condensation nuclei activity and droplet](#)
839 [formation of primary and secondary organic aerosol mixtures, *Aerosol Science and Technology*, 52,
840 \[242–251, <https://doi.org/10.1080/02786826.2017.1392480>, 2018.\]\(#\)](#)

841 Fu, Y., Peng, X., Sun, W., Hu, X., Wang, D., Yang, Y., Guo, Z., Wang, Y., Zhang, G., Zhu, J.,
842 Ou, J., Shi, Z., Wang, X., and Bi, X.: Impact of Cloud Process in the Mixing State and Microphysical
843 Properties of Soot Particles: Implications in Light Absorption Enhancement, *Journal of Geophysical*
844 *Research: Atmospheres*, n/a, e2022JD037169, <https://doi.org/10.1029/2022JD037169>, 2022.

845 Gysel, M., Laborde, M., Olfert, J. S., Subramanian, R., and Gröhn, A. J.: Effective density of
846 Aquadag and fullerene soot black carbon reference materials used for SP2 calibration, *Atmos. Meas.*
847 *Tech.*, 4, 2851–2858, <https://doi.org/10.5194/amt-4-2851-2011>, 2011.

848 [Hennigan, C. J., Westervelt, D. M., Riipinen, I., Engelhart, G. J., Lee, T., Collett Jr., J. L., Pandis,](#)
849 [S. N., Adams, P. J., and Robinson, A. L.: New particle formation and growth in biomass burning](#)
850 [plumes: An important source of cloud condensation nuclei, *Geophysical Research Letters*, 39,
851 \[<https://doi.org/10.1029/2012GL050930>, 2012.\]\(#\)](#)

852 Herich, H., Kammermann, L., Gysel, M., Weingartner, E., Baltensperger, U., Lohmann, U., and
853 Cziczo, D. J.: In situ determination of atmospheric aerosol composition as a function of hygroscopic
854 growth, *Journal of Geophysical Research: Atmospheres*, 113, <https://doi.org/10.1029/2008JD009954>,
855 2008.

856 Herich, H., Kammermann, L., Friedman, B., Gross, D. S., Weingartner, E., Lohmann, U.,
857 Spichtinger, P., Gysel, M., Baltensperger, U., and Cziczo, D. J.: Subarctic atmospheric aerosol
858 composition: 2. Hygroscopic growth properties, *Journal of Geophysical Research: Atmospheres*, 114,
859 <https://doi.org/10.1029/2008JD011574>, 2009.

860 [Hersey, S. P., Craven, J. S., Metcalf, A. R., Lin, J., Latham, T., Suski, K. J., Cahill, J. F., Duong,](#)
861 [H. T., Sorooshian, A., Jonsson, H. H., Shiraiwa, M., Zuend, A., Nenes, A., Prather, K. A., Flagan, R.](#)
862 [C., and Seinfeld, J. H.: Composition and hygroscopicity of the Los Angeles Aerosol: CalNex, *Journal*](#)
863 [of *Geophysical Research: Atmospheres*, 118, 3016–3036, <https://doi.org/10.1002/jgrd.50307>, 2013.](#)

864 [Hodas, N., Zuend, A., et al., 2016. Discontinuities in hygroscopic growth below and above water](#)
865 [saturation for laboratory surrogates of oligomers in organic atmospheric aerosols. *Atmos. Chem. Phys.*](#)
866 [*Discuss.* 1–34, 2016.](#)

867 Hong, J., Äijälä, M., Häme, S. A. K., Hao, L., Duplissy, J., Heikkinen, L. M., Nie, W., Mikkilä,
868 J., Kulmala, M., Prisle, N. L., Virtanen, A., Ehn, M., Paasonen, P., Worsnop, D. R., Riipinen, I., Petäjä,
869 T., and Kerminen, V.-M.: Estimates of the organic aerosol volatility in a boreal forest using two
870 independent methods, *Atmos. Chem. Phys.*, 17, 4387–4399, [https://doi.org/10.5194/acp-17-4387-](https://doi.org/10.5194/acp-17-4387-2017)
871 2017, 2017.

872 Jayne, J. T., Leard, D. C., Zhang, X., Davidovits, P., Smith, K. A., Kolb, C. E., and Worsnop, D.
873 R.: Development of an Aerosol Mass Spectrometer for Size and Composition Analysis of Submicron
874 Particles, *Aerosol Science and Technology*, 33, 49–70, <https://doi.org/10.1080/027868200410840>,
875 2000.

876 Jiang, X., Tao, J., Kuang, Y., Hong, J., and Ma, N.: Mathematical derivation and physical
877 interpretation of particle size-resolved activation ratio based on particle hygroscopicity distribution:
878 Application on global characterization of CCN activity, *Atmospheric Environment*, 246, 118137,
879 <https://doi.org/10.1016/j.atmosenv.2020.118137>, 2021.

880 Jurányi, Z., Tritscher, T., Gysel, M., Laborde, M., Gomes, L., Roberts, G., Baltensperger, U., and
881 Weingartner, E.: Hygroscopic mixing state of urban aerosol derived from size-resolved cloud
882 condensation nuclei measurements during the MEGAPOLI campaign in Paris, *Atmos. Chem. Phys.*,
883 13, 6431–6446, <https://doi.org/10.5194/acp-13-6431-2013>, 2013.

884 Kawana, K., Nakayama, T., and Mochida, M.: Hygroscopicity and CCN activity of atmospheric
885 aerosol particles and their relation to organics: Characteristics of urban aerosols in Nagoya, Japan,
886 *Journal of Geophysical Research: Atmospheres*, 121, 4100–4121,
887 <https://doi.org/10.1002/2015jd023213>, 2016.

888 Kim, N., Yum, S. S., Park, M., Park, J. S., Shin, H. J., and Ahn, J. Y.: Hygroscopicity of urban
889 aerosols and its link to size-resolved chemical composition during spring and summer in Seoul, Korea,
890 *Atmos. Chem. Phys.*, 20, 11245–11262, <https://doi.org/10.5194/acp-20-11245-2020>, 2020.

891 Kuang, Y., Zhao, C. S., Tao, J. C., and Ma, N.: Diurnal variations of aerosol optical properties in
892 the North China Plain and their influences on the estimates of direct aerosol radiative effect, *Atmos.*
893 *Chem. Phys.*, 15, 5761–5772, <https://doi.org/10.5194/acp-15-5761-2015>, 2015.

894 Kuang, Y., He, Y., Xu, W., Yuan, B., Zhang, G., Ma, Z., Wu, C., Wang, C., Wang, S., Zhang, S.,
895 Tao, J., Ma, N., Su, H., Cheng, Y., Shao, M., and Sun, Y.: Photochemical Aqueous-Phase Reactions
896 Induce Rapid Daytime Formation of Oxygenated Organic Aerosol on the North China Plain,
897 *Environmental Science & Technology*, 54, 3849–3860, <https://doi.org/10.1021/acs.est.9b06836>, 2020.

898 Kuang, Y., Huang, S., Xue, B., Luo, B., Song, Q., Chen, W., Hu, W., Li, W., Zhao, P., Cai, M.,
899 Peng, Y., Qi, J., Li, T., Wang, S., Chen, D., Yue, D., Yuan, B., and Shao, M.: Contrasting effects of
900 secondary organic aerosol formations on organic aerosol hygroscopicity, *Atmos. Chem. Phys.*, 21,
901 10375–10391, <https://doi.org/10.5194/acp-21-10375-2021>, 2021.

902 Kuwata, M. and Kondo, Y.: Dependence of size-resolved CCN spectra on the mixing state of
903 nonvolatile cores observed in Tokyo, *Journal of Geophysical Research: Atmospheres*, 113,
904 <https://doi.org/10.1029/2007JD009761>, 2008.

905 Kuwata, M., Kondo, Y., Mochida, M., Takegawa, N., and Kawamura, K.: Dependence of CCN
906 activity of less volatile particles on the amount of coating observed in Tokyo, *Journal of Geophysical*
907 *Research: Atmospheres*, 112, <https://doi.org/10.1029/2006JD007758>, 2007.

908 [Laborde, M.; Crippa, M.; Tritscher, T.; Jurányi, Z.; Decarlo, P. F.; Temime-Roussel, B.; Marchand, N.;](#)
909 [Eckhardt, S.; Stohl, A.; Baltensperger, U.; Prévôt, A. S. H.; Weingartner, E.; Gysel, M. Black carbon](#)
910 [physical properties and mixing state in the European megacity Paris. *Atmos. Chem. Phys.* 2013, 13](#)
911 [\(11\), 5831–5856.](#)

912 Lack, D. A., Langridge, J. M., Bahreini, R., Cappa, C. D., Middlebrook, A. M., and Schwarz, J.
913 P.: Brown carbon and internal mixing in biomass burning particles, *Proceedings of the National*
914 *Academy of Sciences*, 109, 14802–14807, <https://doi.org/10.1073/pnas.1206575109>, 2012.

915 Lance, S., Nenes, A., Medina, J., and Smith, J. N.: Mapping the operation of the DMT continuous
916 flow CCN counter, *Aerosol science and technology*, 40, 242–254, 2006.

917 Lance, S., Raatikainen, T., Onasch, T. B., Worsnop, D. R., Yu, X. Y., Alexander, M. L.,
918 Stolzenburg, M. R., McMurry, P. H., Smith, J. N., and Nenes, A.: Aerosol mixing state, hygroscopic
919 growth and cloud activation efficiency during MIRAGE 2006, *Atmos. Chem. Phys.*, 13, 5049–5062,
920 <https://doi.org/10.5194/acp-13-5049-2013>, 2013.

921 Lata, N. N., Zhang, B., Schum, S., Mazzoleni, L., Brimberry, R., Marcus, M. A., Cantrell, W. H.,
922 Fialho, P., Mazzoleni, C., and China, S.: Aerosol Composition, Mixing State, and Phase State of Free
923 Tropospheric Particles and Their Role in Ice Cloud Formation, *ACS Earth Space Chem.*, 5, 3499–
924 3510, <https://doi.org/10.1021/acsearthspacechem.1c00315>, 2021.

925 Lee, A. K. Y., Rivellini, L.-H., Chen, C.-L., Liu, J., Price, D. J., Betha, R., Russell, L. M., Zhang,
926 X., and Cappa, C. D.: Influences of Primary Emission and Secondary Coating Formation on the
927 Particle Diversity and Mixing State of Black Carbon Particles, *Environ. Sci. Technol.*, 53, 9429–9438,
928 <https://doi.org/10.1021/acs.est.9b03064>, 2019.

929 Li, G., Su, H., Ma, N., Tao, J., Kuang, Y., Wang, Q., Hong, J., Zhang, Y., Kuhn, U., and Zhang,
930 S.: Multiphase chemistry experiment in Fogs and Aerosols in the North China Plain (McFAN):
931 integrated analysis and intensive winter campaign 2018, *Faraday Discussions*, 2021.

932 Liu, D.; [Whitehead, J.; Alfarra, M. R.; Reyes-Villegas, E.; Spracklen, D. V.; Reddington, C. L.;](#)
933 [Kong, S.; Williams, P. I.; Ting, Y.-C.; Haslett, S.; Taylor, J. W.; Flynn, M. J.; Morgan, W. T.;](#)
934 [McFiggans, G.; Coe, H.; Allan, J. D. Black-carbon absorption enhancement in the atmosphere](#)
935 [determined by particle mixing state. *Nat. Geosci.* 2017, 10 \(3\), 184–188.](#)

936 Liu, D., Joshi, R., Wang, J., Yu, C., Allan, J. D., Coe, H., Flynn, M. J., Xie, C., Lee, J., Squires,
937 F., Kotthaus, S., Grimmond, S., Ge, X., Sun, Y., and Fu, P.: Contrasting physical properties of black
938 carbon in urban Beijing between winter and summer, *Atmos. Chem. Phys.*, 19, 6749–6769,
939 <https://doi.org/10.5194/acp-19-6749-2019>, 2019.

940 Liu, D., Li, S., Hu, D., Kong, S., Cheng, Y., Wu, Y., Ding, S., Hu, K., Zheng, S., Yan, Q., Zheng,
941 H., Zhao, D., Tian, P., Ye, J., Huang, M., and Ding, D.: Evolution of Aerosol Optical Properties from
942 Wood Smoke in Real Atmosphere Influenced by Burning Phase and Solar Radiation, *Environ. Sci.*
943 *Technol.*, 55, 5677–5688, <https://doi.org/10.1021/acs.est.0c07569>, 2021.

944 Liu, P., Song, M., et al., 2018. [Resolving the mechanisms of hygroscopic growth and cloud](#)
945 [condensation nuclei activity for organic particulate matter. *Nat. Commun.* 9.](#)

946 Liu, P., Kaplan, J. O., Mickley, L. J., Li, Y., Chellman, N. J., Arienzo, M. M., Kodros, J. K.,
947 [Pierce, J. R., Sigl, M., Freitag, J., Mulvaney, R., Curran, M. A. J., and McConnell, J. R.: Improved](#)
948 [estimates of preindustrial biomass burning reduce the magnitude of aerosol climate forcing in the](#)
949 [Southern Hemisphere, *Science Advances*, 7, 10.1126/sciadv.abc1379, 2021.](#)

950 [Liu, K.](#), Zhang, C., Cheng, Y., Liu, C., Zhang, H., Zhang, G., Sun, X., and Mu, Y.: Serious BTEX
951 pollution in rural area of the North China Plain during winter season, *Journal of Environmental*
952 *Sciences*, 30, 186–190, <https://doi.org/10.1016/j.jes.2014.05.056>, 2015.

953 Liu, P. F., Zhao, C. S., Göbel, T., Hallbauer, E., Nowak, A., Ran, L., Xu, W. Y., Deng, Z. Z., Ma,
954 N., and Mildenberger, K.: Hygroscopic properties of aerosol particles at high relative humidity and
955 their diurnal variations in the North China Plain, *Atmos. Chem. Phys.*, 11, 3479–3494, 2011.

956 Luo, B., Kuang, Y., Huang, S., Song, Q., Hu, W., Li, W., Peng, Y., Chen, D., Yue, D., Yuan, B.,
957 and Shao, M.: Parameterizations of size distribution and refractive index of biomass burning organic
958 aerosol with black carbon content, *Atmos. Chem. Phys.*, 22, 12401–12415,
959 <https://doi.org/10.5194/acp-22-12401-2022>, 2022.

960 Ma, N., Zhao, C. S., Müller, T., Cheng, Y. F., Liu, P. F., Deng, Z. Z., Xu, W. Y., Ran, L., Nekat,
961 B., van Pinxteren, D., Gnauk, T., Müller, K., Herrmann, H., Yan, P., Zhou, X. J., and Wiedensohler,
962 A.: A new method to determine the mixing state of light absorbing carbonaceous using the measured
963 aerosol optical properties and number size distributions, *Atmos. Chem. Phys.*, 12, 2381–2397,
964 <https://doi.org/10.5194/acp-12-2381-2012>, 2012.

965 Ma, N., Zhao, C., Tao, J., Wu, Z., Kecorius, S., Wang, Z., Größ, J., Liu, H., Bian, Y., Kuang, Y.,
966 Teich, M., Spindler, G., Müller, K., van Pinxteren, D., Herrmann, H., Hu, M., and Wiedensohler, A.:
967 Variation of CCN activity during new particle formation events in the North China Plain, *Atmos. Chem.*
968 *Phys.*, 16, 8593–8607, <https://doi.org/10.5194/acp-16-8593-2016>, 2016.

969 [Malek, K. A., Gohil, K., Al-Abadleh, H. A., and Asa-Awuku, A. A.: Hygroscopicity of](#)
970 [polycatechol and polyguaiacol secondary organic aerosol in sub- and supersaturated water vapor](#)
971 [environments††Electronic supplementary information \(ESI\) available: Detailed experimental](#)
972 [procedures, and figures and tables showing data analysis. See DOI: 10.1039/d1ea00063b,](#)
973 [Environmental Science: Atmospheres, 2, 24–33, https://doi.org/10.1039/d1ea00063b, 2022.](#)

974 [May, A. A., Levin, E. J. T., Hennigan, C. J., Riipinen, I., Lee, T., Collett Jr., J. L., Jimenez, J. L.,](#)
975 [Kreidenweis, S. M., and Robinson, A. L.: Gas-particle partitioning of primary organic aerosol](#)
976 [emissions: 3. Biomass burning, Journal of Geophysical Research: Atmospheres, 118, 11,327-11,338,](#)
977 [https://doi.org/10.1002/jgrd.50828, 2013.](#)

978 Matsui, H., Hamilton, D. S., and Mahowald, N. M.: Black carbon radiative effects highly sensitive
979 to emitted particle size when resolving mixing-state diversity, *Nature Communications*, 9, 3446,
980 <https://doi.org/10.1038/s41467-018-05635-1>, 2018.

981 Mei, F., Hayes, P. L., Ortega, A., Taylor, J. W., Allan, J. D., Gilman, J., Kuster, W., de Gouw, J.,
982 Jimenez, J. L., and Wang, J.: Droplet activation properties of organic aerosols observed at an urban
983 site during CalNex-LA, *Journal of Geophysical Research-Atmospheres*, 118, 2903–2917,
984 <https://doi.org/10.1002/jgrd.50285>, 2013.

985 Metcalf, A. R., Craven, J. S., Ensberg, J. J., Brioude, J., Angevine, W., Sorooshian, A., Duong,
986 H. T., Jonsson, H. H., Flagan, R. C., and Seinfeld, J. H.: Black carbon aerosol over the Los Angeles
987 Basin during CalNex, *Journal of Geophysical Research: Atmospheres*, 117,
988 <https://doi.org/10.1029/2011JD017255>, 2012.

989 Middlebrook, A. M., Bahreini, R., Jimenez, J. L., and Canagaratna, M. R.: Evaluation of
990 Composition-Dependent Collection Efficiencies for the Aerodyne Aerosol Mass Spectrometer using
991 Field Data, *Aerosol Science and Technology*, 46, 258–271,
992 <https://doi.org/10.1080/02786826.2011.620041>, 2012.

993 Moffet, R. C., O'Brien, R. E., Alpert, P. A., Kelly, S. T., Pham, D. Q., Gilles, M. K., Knopf, D.
994 A., and Laskin, A.: Morphology and mixing of black carbon particles collected in central California
995 during the CARES field study, *Atmos. Chem. Phys.*, 16, 14515–14525, [https://doi.org/10.5194/acp-](https://doi.org/10.5194/acp-16-14515-2016)
996 [16-14515-2016](https://doi.org/10.5194/acp-16-14515-2016), 2016.

997 Mohr, C., Huffman, J. A., Cubison, M. J., Aiken, A. C., Docherty, K. S., Kimmel, J. R., Ulbrich,
998 I. M., Hannigan, M., and Jimenez, J. L.: Characterization of Primary Organic Aerosol Emissions from
999 Meat Cooking, Trash Burning, and Motor Vehicles with High-Resolution Aerosol Mass Spectrometry
1000 and Comparison with Ambient and Chamber Observations, *Environ. Sci. Technol.*, 43, 2443–2449,
1001 <https://doi.org/10.1021/es8011518>, 2009.

1002 Moteki, N. and Kondo, Y.: Effects of Mixing State on Black Carbon Measurements by Laser-
1003 Induced Incandescence, *Aerosol Science and Technology*, 41, 398–417,
1004 <https://doi.org/10.1080/02786820701199728>, 2007.

1005 [Mukherjee, S., Anil Kumar, V., Patil, R. D., Meena, G. S., Buchunde, P., Waghmare, V.,](#)
1006 [Deshmukh, S., Dhavale, V., Ray, A., Panicker, A. S., Sonbawne, S. M., Safai, P. D., and Pandithurai,](#)
1007 [G.: Investigation of physico-chemical characteristics and associated CCN activation for different](#)
1008 [combustion sources through Chamber experiment approach, *Atmospheric Environment*, 266, 118726,](#)
1009 [<https://doi.org/10.1016/j.atmosenv.2021.118726>, 2021.](#)

1010 Nordmann, S., Cheng, Y. F., Carmichael, G. R., Yu, M., Denier van der Gon, H. A. C., Zhang,
1011 Q., Saide, P. E., Pöschl, U., Su, H., Birmili, W., and Wiedensohler, A.: Atmospheric black carbon and
1012 warming effects influenced by the source and absorption enhancement in central Europe, *Atmos. Chem.*
1013 *Phys.*, 14, 12683–12699, <https://doi.org/10.5194/acp-14-12683-2014>, 2014.

1014 [Ovadnevaite, J., Zuend, A., Laaksonen, A., Sanchez, K.J., Roberts, G., Ceburnis, D., Decesari,](#)
1015 [S., Rinaldi, M., Hodas, N., Facchini, M.C., Seinfeld, J.H., O' Dowd, C., 2017. Surface tension prevails](#)
1016 [over solute effect in organic-influenced cloud droplet activation. *Nature* 546, 637–641.](#)
1017 [<https://doi.org/10.1038/nature22806>.](#)

1018 Paatero, P. and Tapper, U.: Positive matrix factorization: A non-negative factor model with
1019 optimal utilization of error estimates of data values, *Environmetrics*, 5, 111–126,
1020 <https://doi.org/10.1002/env.3170050203>, 1994.

1021 [Pajunoja, A., Lambe, A.T., Hakala, J., Rastak, N., Cummings, M.J., Brogan, J.F., Hao, L.,](#)
1022 [Paramonov, M., Hong, J., Prisle, N.L., Malila, J., Romakkaniemi, S., Lehtinen, K.E.J., Laaksonen, A.,](#)
1023 [Kulmala, M., Massoli, P., Onasch, T.B., Donahue, N.M., Riipinen, I., Davidovits, P., Worsnop, D.R.,](#)
1024 [Petaja, T., Virtanen, A., 2015. Adsorptive uptake of water by semisolid secondary organic aerosols.](#)
1025 [*Geophys. Res. Lett.* 42, 3063–3068. <https://doi.org/10.1002/2015GL063142>.](#)

1026 Peng, J., Hu, M., Guo, S., Du, Z., Zheng, J., Shang, D., Levy Zamora, M., Zeng, L., Shao, M.,
1027 Wu, Y.-S., Zheng, J., Wang, Y., Glen, C. R., Collins, D. R., Molina, M. J., and Zhang, R.: Markedly
1028 enhanced absorption and direct radiative forcing of black carbon under polluted urban environments,

1029 Proceedings of the National Academy of Sciences, 113, 4266–4271,
1030 <https://doi.org/10.1073/pnas.1602310113>, 2016.

1031 [Pöhlker, M. L., Ditas, F., Saturno, J., Klimach, T., Hrabě de Angelis, I., Araùjo, A. C., Brito, J.,](#)
1032 [Carbone, S., Cheng, Y., Chi, X., Ditz, R., Gunthe, S. S., Holanda, B. A., Kandler, K., Kesselmeier, J.,](#)
1033 [Könemann, T., Krüger, O. O., Lavrič, J. V., Martin, S. T., Mikhailov, E., Moran-Zuloaga, D., Rizzo,](#)
1034 [L. V., Rose, D., Su, H., Thalman, R., Walter, D., Wang, J., Wolff, S., Barbosa, H. M. J., Artaxo, P.,](#)
1035 [Andreae, M. O., Pöschl, U., and Pöhlker, C.: Long-term observations of cloud condensation nuclei](#)
1036 [over the Amazon rain forest – Part 2: Variability and characteristics of biomass burning, long-range](#)
1037 [transport, and pristine rain forest aerosols, Atmos. Chem. Phys., 18, 10289–10331,](#)
1038 <https://doi.org/10.5194/acp-18-10289-2018>, 2018.

1039 [Pöhlker, M. L., Pöhlker, C., Quaas, J., Mülmenstädt, J., Pozzer, A., Andreae, M. O., Artaxo, P.,](#)
1040 [Block, K., Coe, H., Ervens, B., Gallimore, P., Gaston, C. J., Gunthe, S. S., Henning, S., Herrmann, H.,](#)
1041 [Krüger, O. O., McFiggans, G., Poulain, L., Raj, S. S., Reyes-Villegas, E., Royer, H. M., Walter, D.,](#)
1042 [Wang, Y., and Pöschl, U.: Global organic and inorganic aerosol hygroscopicity and its effect on](#)
1043 [radiative forcing, Nature communications, 14, 6139, 10.1038/s41467-023-41695-8, 2023](#)

1044 Philippin, S., Wiedensohler, A., and Stratmann, F.: Measurements of non-volatile fractions of
1045 pollution aerosols with an eight-tube volatility tandem differential mobility analyzer (VTDMA-8),
1046 Journal of Aerosol Science, 35, 185–203, <https://doi.org/10.1016/j.jaerosci.2003.07.004>, 2004.

1047 [Qiu, Y., Xie, Q., Wang, J., Xu, W., Li, L., Wang, Q., Zhao, J., Chen, Y., Chen, Y., Wu, Y., Du,](#)
1048 [W., Zhou, W., Lee, J., Zhao, C., Ge, X., Fu, P., Wang, Z., Worsnop, D. R., and Sun, Y.: Vertical](#)
1049 [Characterization and Source Apportionment of Water-Soluble Organic Aerosol with High-resolution](#)
1050 [Aerosol Mass Spectrometry in Beijing, China, ACS Earth Space Chem., 3, 273–284,](#)
1051 <https://doi.org/10.1021/acsearthspacechem.8b00155>, 2019.

1052 Ren, J., Zhang, F., Wang, Y., Collins, D., Fan, X., Jin, X., Xu, W., Sun, Y., Cribb, M., and Li, Z.:
1053 Using different assumptions of aerosol mixing state and chemical composition to predict CCN
1054 concentrations based on field measurements in urban Beijing, Atmospheric Chemistry and Physics,
1055 18, 6907–6921, <https://doi.org/10.5194/acp-18-6907-2018>, 2018.

1056 Riemer, N., Ault, A. P., West, M., Craig, R. L., and Curtis, J. H.: Aerosol Mixing State:
1057 Measurements, Modeling, and Impacts, Reviews of Geophysics, 57, 187–249,
1058 <https://doi.org/10.1029/2018RG000615>, 2019.

1059 Roberts, G. C. and Nenes, A.: A continuous-flow streamwise thermal-gradient CCN chamber for
1060 atmospheric measurements, Aerosol science and technology, 39, 206–221, 2005.

1061 Rose, D., Gunthe, S. S., Mikhailov, E., Frank, G. P., Dusek, U., Andreae, M. O., and Pöschl, U.:
1062 Calibration and measurement uncertainties of a continuous-flow cloud condensation nuclei counter
1063 (DMT-CCNC): CCN activation of ammonium sulfate and sodium chloride aerosol particles in theory
1064 and experiment, Atmos. Chem. Phys., 8, 1153–1179, 2008.

1065 Rose, D., Nowak, A., Achtert, P., Wiedensohler, A., Hu, M., Shao, M., Zhang, Y., Andreae, M.
1066 O., and Pöschl, U.: Cloud condensation nuclei in polluted air and biomass burning smoke near the
1067 mega-city Guangzhou, China - Part 1: Size-resolved measurements and implications for the modeling
1068 of aerosol particle hygroscopicity and CCN activity, Atmos. Chem. Phys., 10, 3365–3383, 2010.

1069 Rose, D., Gunthe, S. S., Su, H., Garland, R. M., Yang, H., Berghof, M., Cheng, Y. F., Wehner,
1070 B., Achtert, P., Nowak, A., Wiedensohler, A., Takegawa, N., Kondo, Y., Hu, M., Zhang, Y., Andreae,
1071 M. O., and Poschl, U.: Cloud condensation nuclei in polluted air and biomass burning smoke near the
1072 mega-city Guangzhou, China -Part 2: Size-resolved aerosol chemical composition, diurnal cycles, and
1073 externally mixed weakly CCN-active soot particles, *Atmos. Chem. Phys.*, 11, 2817–2836,
1074 <https://doi.org/10.5194/acp-11-2817-2011>, 2011.

1075 [Ruehl, C.R., Davies, J.F., Wilson, K.R., 2016. An interfacial mechanism for cloud droplet](#)
1076 [formation on organic aerosols. *Science* 351, 1447–1450, 6280.](#)

1077 Saha, P. K., Khlystov, A., and Grieshop, A. P.: Downwind evolution of the volatility and mixing
1078 state of near-road aerosols near a US interstate highway, *Atmos. Chem. Phys.*, 18, 2139–2154,
1079 <https://doi.org/10.5194/acp-18-2139-2018>, 2018.

1080 [Schwarz, J. P.; Gao, R. S.; Spackman, J. R.; Watts, L. A.; Thomson, D. S.; Fahey, D. W.; Ryerson,](#)
1081 [T. B.; Peischl, J.; Holloway, J. S.; Trainer, M.; Frost, G. J.; Baynard, T.; Lack, D. A.; de Gouw, J. A.;](#)
1082 [Warneke, C.; Del Negro, L. A. Measurement of the mixing state, mass, and optical size of individual](#)
1083 [black carbon particles in urban and biomass burning emissions. *Geophys. Res. Lett.* 2008, 35, L13810.](#)

1084 Sedlacek, A. J., Lewis, E. R., Kleinman, L., Xu, J., and Zhang, Q.: Determination of and evidence
1085 for non-core-shell structure of particles containing black carbon using the Single-Particle Soot
1086 Photometer (SP2), *Geophysical Research Letters*, 39, L06802, <https://doi.org/10.1029/2012GL050905>,
1087 2012.

1088 Shi, J., Hong, J., Ma, N., Luo, Q., He, Y., Xu, H., Tan, H., Wang, Q., Tao, J., Zhou, Y., Han, S.,
1089 Peng, L., Xie, L., Zhou, G., Xu, W., Sun, Y., Cheng, Y., and Su, H.: Measurement report: On the
1090 difference in aerosol hygroscopicity between high and low relative humidity conditions in the North
1091 China Plain, *Atmos. Chem. Phys.*, 22, 4599–4613, <https://doi.org/10.5194/acp-22-4599-2022>, 2022.

1092 [Spracklen, D. V., Carslaw, K. S., Pošchl, U., Rap, A., and Forster, P. M.: Global cloud](#)
1093 [condensation nuclei influenced by carbonaceous combustion aerosol, *Atmos. Chem. Phys.*, 11, 9067–](#)
1094 [9087, doi:10.5194/acp-11-9067-2011, 2011.](#)

1095 Stevens, R., Ryjkov, A., Majdzadeh, M., and Dastoor, A.: An improved representation of aerosol
1096 mixing state for air quality–weather interactions, *Atmos. Chem. Phys.*, 22, 13527–13549,
1097 <https://doi.org/10.5194/acp-22-13527-2022>, 2022.

1098 Stolzenburg, M. R. and McMurry, P. H.: Equations governing single and tandem DMA
1099 configurations and a new lognormal approximation to the transfer function, *Aerosol Science and*
1100 *Technology*, 42, 421–432, 2008.

1101 Su, H., Rose, D., Cheng, Y. F., Gunthe, S. S., Massling, A., Stock, M., Wiedensohler, A., Andreae,
1102 M. O., and Poschl, U.: Hygroscopicity distribution concept for measurement data analysis and
1103 modeling of aerosol particle mixing state with regard to hygroscopic growth and CCN activation,
1104 *Atmos. Chem. Phys.*, 10, 7489–7503, <https://doi.org/10.5194/acp-10-7489-2010>, 2010.

1105 Subramanian, R., Kok, G. L., Baumgardner, D., Clarke, A., Shinozuka, Y., Campos, T. L., Heizer,
1106 C. G., Stephens, B. B., de Foy, B., Voss, P. B., and Zaveri, R. A.: Black carbon over Mexico: the effect
1107 of atmospheric transport on mixing state, mass absorption cross-section, and BC/CO ratios, *Atmos.*
1108 *Chem. Phys.*, 10, 219–237, <https://doi.org/10.5194/acp-10-219-2010>, 2010.

- 1109 Tan, H., Xu, H., Wan, Q., Li, F., Deng, X., Chan, P. W., Xia, D., and Yin, Y.: Design and
1110 Application of an Unattended Multifunctional H-TDMA System, *Journal of Atmospheric and Oceanic*
1111 *Technology*, 30, 1136–1148, <https://doi.org/10.1175/JTECH-D-12-00129.1>, 2013.
- 1112 Tao, J., Zhao, C., Nan, M., and Ye, K.: Consistency and applicability of parameterization schemes
1113 for the size-resolved aerosol activation ratio based on field measurements in the North China Plain,
1114 *Atmospheric Environment*, 173, 316–324, 2018.
- 1115 Tao, J., Kuang, Y., Ma, N., Zheng, Y., Wiedensohler, A., and Zhao, C.: An improved
1116 parameterization scheme for size-resolved particle activation ratio and its application on comparison
1117 study of particle hygroscopicity measurements between HTDMA and DMA-CCNC, *Atmospheric*
1118 *Environment*, 226, 117403, <https://doi.org/10.1016/j.atmosenv.2020.117403>, 2020.
- 1119 Tao, J., Kuang, Y., Ma, N., Hong, J., Sun, Y., Xu, W., Zhang, Y., He, Y., Luo, Q., Xie, L., Su,
1120 H., and Cheng, Y.: Secondary aerosol formation alters CCN activity in the North China Plain, *Atmos.*
1121 *Chem. Phys.*, 21, 7409–7427, <https://doi.org/10.5194/acp-21-7409-2021>, 2021.
- 1122 Tao, M., Chen, L., Su, L., and Tao, J.: Satellite observation of regional haze pollution over the
1123 North China Plain, *Journal of Geophysical Research: Atmospheres*, 117,
1124 <https://doi.org/10.1029/2012JD017915>, 2012.
- 1125 Thalman, R., de Sa, S. S., Palm, B. B., Barbosa, H. M. J., Poehlker, M. L., Alexander, M. L.,
1126 Brito, J., Carbone, S., Castillo, P., Day, D. A., Kuang, C., Manzi, A., Ng, N. L., Sedlacek, A. J., Souza,
1127 R., Springston, S., Watson, T., Poehlker, C., Poeschl, U., Andreae, M. O., Artaxo, P., Jimenez, J. L.,
1128 Martin, S. T., and Wang, J.: CCN activity and organic hygroscopicity of aerosols downwind of an
1129 urban region in central Amazonia: seasonal and diel variations and impact of anthropogenic emissions,
1130 *Atmospheric Chemistry and Physics*, 17, 11779–11801, <https://doi.org/10.5194/acp-17-11779-2017>,
1131 2017.
- 1132 Ting, Y., Mitchell, E. J. S., Allan, J. D., Liu, D., Spracklen, D. V., Williams, A., Jones, J. M.,
1133 Lea-Langton, A. R., McFiggans, G., and Coe, H.: Mixing State of Carbonaceous Aerosols of Primary
1134 Emissions from “Improved” African Cookstoves, *Environ. Sci. Technol.*, 52, 10134–10143,
1135 <https://doi.org/10.1021/acs.est.8b00456>, 2018.
- 1136 Tomlin, J. M., Jankowski, K. A., Veghte, D. P., China, S., Wang, P., Fraund, M., Weis, J., Zheng,
1137 G., Wang, Y., Rivera-Adorno, F., Raveh-Rubin, S., Knopf, D. A., Wang, J., Gilles, M. K., Moffet, R.
1138 C., and Laskin, A.: Impact of dry intrusion events on the composition and mixing state of particles
1139 during the winter Aerosol and Cloud Experiment in the Eastern North Atlantic (ACE-ENA), *Atmos.*
1140 *Chem. Phys.*, 21, 18123–18146, <https://doi.org/10.5194/acp-21-18123-2021>, 2021.
- 1141 Ulbrich, I. M., Canagaratna, M. R., Zhang, Q., Worsnop, D. R., and Jimenez, J. L.: Interpretation
1142 of organic components from Positive Matrix Factorization of aerosol mass spectrometric data, *Atmos.*
1143 *Chem. Phys.*, 9, 2891–2918, <https://doi.org/10.5194/acp-9-2891-2009>, 2009.
- 1144 [Vu, D., Short, D., Karavalakis, G., Durbin, T. D., and Asa-Awuku, A.: Integrating Cloud](https://doi.org/10.1080/02786826.2015.1105358)
1145 [Condensation Nuclei Predictions with Fast Time Resolved Aerosol Instrumentation to Determine the](https://doi.org/10.1080/02786826.2015.1105358)
1146 [Hygroscopic Properties of Emissions Over Transient Drive Cycles, *Aerosol Science and Technology*,](https://doi.org/10.1080/02786826.2015.1105358)
1147 [49, 1149–1159, https://doi.org/10.1080/02786826.2015.1105358, 2015.](https://doi.org/10.1080/02786826.2015.1105358)

1148 [Vu, D., Short, D., Karavalakis, G., Durbin, T. D., and Asa-Awuku, A.: Will Aerosol](#)
1149 [Hygroscopicity Change with Biodiesel, Renewable Diesel Fuels and Emission Control Technologies?,](#)
1150 [Environ. Sci. Technol., 51, 1580–1586, <https://doi.org/10.1021/acs.est.6b03908>, 2017.](#)

1151 Wang, X., Ye, X., Chen, J., Wang, X., Yang, X., Fu, T.-M., Zhu, L., and Liu, C.: Direct links
1152 between hygroscopicity and mixing state of ambient aerosols: estimating particle hygroscopicity from
1153 their single-particle mass spectra, *Atmos. Chem. Phys.*, 20, 6273–6290, [https://doi.org/10.5194/acp-](https://doi.org/10.5194/acp-20-6273-2020)
1154 [20-6273-2020](https://doi.org/10.5194/acp-20-6273-2020), 2020.

1155 Wang, Y., Wang, X., Kondo, Y., Kajino, M., Munger, J. W., and Hao, J.: Black carbon and its
1156 correlation with trace gases at a rural site in Beijing: Top-down constraints from ambient
1157 measurements on bottom-up emissions, *Journal of Geophysical Research: Atmospheres*, 116,
1158 <https://doi.org/10.1029/2011JD016575>, 2011.

1159 Wang, Y., Zhang, F., Li, Z., Tan, H., Xu, H., Ren, J., Zhao, J., Du, W., and Sun, Y.: Enhanced
1160 hydrophobicity and volatility of submicron aerosols under severe emission control conditions in
1161 Beijing, *Atmos. Chem. Phys.*, 17, 5239–5251, <https://doi.org/10.5194/acp-17-5239-2017>, 2017.

1162 Wang, Y., Hu, R., Wang, Q., Li, Z., Cribb, M., Sun, Y., Song, X., Shang, Y., Wu, Y., Huang, X.,
1163 and Wang, Y.: Different effects of anthropogenic emissions and aging processes on the mixing state
1164 of soot particles in the nucleation and accumulation modes, *Atmos. Chem. Phys.*, 22, 14133–14146,
1165 <https://doi.org/10.5194/acp-22-14133-2022>, 2022.

1166 Wehner, B., Berghof, M., Cheng, Y. F., Achtert, P., Birmili, W., Nowak, A., Wiedensohler, A.,
1167 Garland, R. M., Pöschl, U., Hu, M., and Zhu, T.: Mixing state of nonvolatile aerosol particle fractions
1168 and comparison with light absorption in the polluted Beijing region, *Journal of Geophysical Research:*
1169 *Atmospheres*, 114, <https://doi.org/10.1029/2008JD010923>, 2009.

1170 [Wex, H., Petters, M.D., et al., 2009. Towards closing the gap between hygroscopic growth and](#)
1171 [activation for secondary organic aerosol: Part 1-Evidence from measurements. *Atmos. Chem. Phys.* 9](#)
1172 [\(12\), 3987–3997.](#)

1173 Wu, Y., Wang, X., Tao, J., Huang, R., Tian, P., Cao, J., Zhang, L., Ho, K.-F., Han, Z., and Zhang,
1174 R.: Size distribution and source of black carbon aerosol in urban Beijing during winter haze episodes,
1175 *Atmos. Chem. Phys.*, 17, 7965–7975, <https://doi.org/10.5194/acp-17-7965-2017>, 2017.

1176 Xu, W., Sun, Y., Wang, Q., Zhao, J., Wang, J., Ge, X., Xie, C., Zhou, W., Du, W., Li, J., Fu, P.,
1177 Wang, Z., Worsnop, D. R., and Coe, H.: Changes in Aerosol Chemistry From 2014 to 2016 in Winter
1178 in Beijing: Insights From High-Resolution Aerosol Mass Spectrometry, *Journal of Geophysical*
1179 *Research: Atmospheres*, 124, 1132–1147, <https://doi.org/10.1029/2018JD029245>, 2019.

1180 Xu, W. Y., Zhao, C. S., Ran, L., Deng, Z. Z., Liu, P. F., Ma, N., Lin, W. L., Xu, X. B., Yan, P.,
1181 He, X., Yu, J., Liang, W. D., and Chen, L. L.: Characteristics of pollutants and their correlation to
1182 meteorological conditions at a suburban site in the North China Plain, *Atmos. Chem. Phys.*, 11, 4353–
1183 4369, <https://doi.org/10.5194/acp-11-4353-2011>, 2011.

1184 Yang, Z., Ma, N., Wang, Q., Li, G., Pan, X., Dong, W., Zhu, S., Zhang, S., Gao, W., He, Y., Xie,
1185 L., Zhang, Y., Kuhn, U., Xu, W., Kuang, Y., Tao, J., Hong, J., Zhou, G., Sun, Y., Su, H., and Cheng,
1186 Y.: Characteristics and source apportionment of black carbon aerosol in the North China Plain,
1187 *Atmospheric Research*, 276, 106246, <https://doi.org/10.1016/j.atmosres.2022.106246>, 2022.

1188 Zhang, F., Li, Y., Li, Z., Sun, L., Li, R., Zhao, C., Wang, P., Sun, Y., Liu, X., Li, J., Li, P., Ren,
1189 G., and Fan, T.: Aerosol hygroscopicity and cloud condensation nuclei activity during the AC3Exp
1190 campaign: implications for cloud condensation nuclei parameterization, *Atmos. Chem. Phys.*, 14,
1191 13423–13437, <https://doi.org/10.5194/acp-14-13423-2014>, 2014.

1192 [Zhang, F., Wang, Y., Peng, J., Chen, L., Sun, Y., Duan, L., Ge, X., Li, Y., Zhao, J., Liu, C., Zhang,
1193 X., Zhang, G., Pan, Y., Wang, Y., Zhang, A. L., Ji, Y., Wang, G., Hu, M., Molina, M. J., and Zhang,
1194 R.: An unexpected catalyst dominates formation and radiative forcing of regional haze, *Proceedings
1195 of the National Academy of Sciences*, 117, 3960–3966, <https://doi.org/10.1073/pnas.1919343117>,
1196 2020.](#)

1197 [Zhang, G., Fu, Y., Peng, X., Sun, W., Shi, Z., Song, W., Hu, W., Chen, D., Lian, X., Li, L., Tang,
1198 M., Wang, X., and Bi, X.: Black Carbon Involved Photochemistry Enhances the Formation of Sulfate
1199 in the Ambient Atmosphere: Evidence From In Situ Individual Particle Investigation, *Journal of
1200 Geophysical Research: Atmospheres*, 126, e2021JD035226, <https://doi.org/10.1029/2021JD035226>,
1201 2021.](#)

1202 [Zhang, S., Shen, X., Sun, J., Zhang, Y., Zhang, X., Xia, C., Hu, X., Zhong, J., Wang, J., and Liu,
1203 S.: Atmospheric Particle Hygroscopicity and the Influence by Oxidation State of Organic Aerosols in
1204 Urban Beijing, *Journal of Environmental Sciences*, 124, 544–556,
1205 <https://doi.org/10.1016/j.jes.2021.11.019>, 2023.](#)

1206 Zhang, S. L., Ma, N., Kecorius, S., Wang, P. C., Hu, M., Wang, Z. B., Größ, J., Wu, Z. J., and
1207 Wiedensohler, A.: Mixing state of atmospheric particles over the North China Plain, *Atmospheric
1208 Environment*, 125, 152–164, 2016.

1209 Zhang, Y., Su, H., Ma, N., Li, G., Kecorius, S., Wang, Z., Hu, M., Zhu, T., He, K., Wiedensohler,
1210 A., Zhang, Q., and Cheng, Y.: Sizing of Ambient Particles From a Single-Particle Soot Photometer
1211 Measurement to Retrieve Mixing State of Black Carbon at a Regional Site of the North China Plain,
1212 *Journal of Geophysical Research: Atmospheres*, 123, 12,778–12,795,
1213 <https://doi.org/10.1029/2018JD028810>, 2018.

1214 [Zhang, Y., Yuan, Q., Huang, D., Kong, S., Zhang, J., Wang, X., Lu, C., Shi, Z., Zhang, X., Sun,
1215 Y., Wang, Z., Shao, L., Zhu, J., and Li, W.: Direct Observations of Fine Primary Particles From
1216 Residential Coal Burning: Insights Into Their Morphology, Composition, and Hygroscopicity, *Journal
1217 of Geophysical Research: Atmospheres*, 123, 12,964–12,979, <https://doi.org/10.1029/2018JD028988>,
1218 2018.](#)

1219 [Zhang, Y., Zhang, Q., Yao, Z., & Li, H. \(2020\). Particle Size and Mixing State of Freshly Emitted
1220 Black Carbon from Different Combustion Sources in China. *Environmental Science & Technology*,
1221 54\(13\), 7766–7774. <https://doi.org/10.1021/acs.est.9b07373>](#)

1222 Zhao, G., Tao, J., Kuang, Y., Shen, C., Yu, Y., and Zhao, C.: Role of black carbon mass size
1223 distribution in the direct aerosol radiative forcing, *Atmos. Chem. Phys.*, 19, 13175–13188,
1224 <https://doi.org/10.5194/acp-19-13175-2019>, 2019.

1225 Zhao, G., Tan, T., Hu, S., Du, Z., Shang, D., Wu, Z., Guo, S., Zheng, J., Zhu, W., Li, M., Zeng,
1226 L., and Hu, M.: Mixing state of black carbon at different atmospheres in north and southwest China,
1227 *Atmos. Chem. Phys.*, 22, 10861–10873, <https://doi.org/10.5194/acp-22-10861-2022>, 2022.

1228 Zheng, H., Kong, S., Wu, F., Cheng, Y., Niu, Z., Zheng, S., Yang, G., Yao, L., Yan, Q., Wu, J.,
1229 Zheng, M., Chen, N., Xu, K., Yan, Y., Liu, D., Zhao, D., Zhao, T., Bai, Y., Li, S., and Qi, S.: Intra-
1230 regional transport of black carbon between the south edge of the North China Plain and central China
1231 during winter haze episodes, *Atmos. Chem. Phys.*, 19, 4499–4516, [https://doi.org/10.5194/acp-19-](https://doi.org/10.5194/acp-19-4499-2019)
1232 4499-2019, 2019.

1233 Zhuang, B. L., Li, S., Wang, T. J., Deng, J. J., Xie, M., Yin, C. Q., and Zhu, J. L.: Direct radiative
1234 forcing and climate effects of anthropogenic aerosols with different mixing states over China,
1235 *Atmospheric Environment*, 79, 349–361, <https://doi.org/10.1016/j.atmosenv.2013.07.004>, 2013.

Table 1. Definition and description of abbreviations.

Abbreviation	Full name and/or Definition
	Biomass Burning Organic Aerosol
BBOA	Characterized by obvious m/z 60 (mainly C ₂ H ₄ O ₂ ⁺) and 73 (mainly C ₃ H ₅ O ₂ ⁺), which are two indicators of biomass burning
	Fossil Fuel Organic Aerosol
FFOA	A mixed factor that comprises traffic emissions and coal combustion, which was characterized by typical hydrocarbon ion series
	Oxygenated Organic Aerosol
OOA1 and OOA2	Two OOA factors resolved from the PMF analysis
	Secondary Organic Aerosol
SOA	Summation of OOA1 and OOA2
	Primary Organic Aerosol
POA	Summation of BBOA and FFOA
	Secondary Inorganic Aerosols, including nitrate, sulfate, and ammonium
SIA	
	Particulate Matter with an aerodynamic <u>Midpoint activation</u> diameter
PM _{2.5} <u>D_a</u>	<2.5 μm
	<u>Linked to the hygroscopicity of CCNs</u>
	Particulate Matter with an aerodynamic diameter <1 μm
PM ₁	
NR-PM ₁	Non-refractory PM₁
	Mass Fraction
MF	
	Particle diameter after humidification or heating
D _p	
	Particle diameter under dry conditions without humidification or heating
D _d	
	<u>Particle diameter after humidification or heating</u>
D _p	
	Growth factor
GF	<u>The ratio between particles with and without humidification and is linked to aerosol hygroscopicity</u>

κ	Hygroscopicity parameter
SSMF	Supersaturation Mass Fraction
SPAR	Size-resolved Particle Activation Ratio
	Size-dependent CCN activity under a specific SS
	Maximum Activation Fraction
MAF	An asymptote of the measured SPAR curve at large particle sizes and represents the number fraction of CCNs to total particles
	Midpoint activation diameter
D_a N_{FH}	Linked to the hygroscopicity of CCNs Number Fraction of Hydrophilic aerosol whose hygroscopicity parameter is $> \sim 0.07$ at particle size of 50, 100, 150 and 200 nm
N_{FV}	Number Fraction of Volatile aerosol whose Shrinkage Factor at 200 °C is < 0.85 at particle size of 50, 100, 150 and 200 nm
N_{FnoBC}	Number Fraction of black carbon (BC)-free particles at particle size of 200, 250, 300 and 370 nm
N_{FCBC}	Number Fraction of thickly coated BC particles at particle size of 200, 250, 300 and 370 nm
$N_{FA} - N_{FB}$	The difference between the number fraction of A and B at particle size of 200 nm
$(N_{FnoBC} - N_{FH}, N_{FV} - N_{FH}, N_{FnoBC} - N_{FV}, N_{FV} - MAF, N_{FnoBC} - MAF)$	
OOA1 and OOA2	Two OOA factors resolved from the PMF analysis
PDF	Probability Distribution Function
PM_{2.5}	Particulate Matter with an aerodynamic diameter $< 2.5 \mu\text{m}$
PM₁	Particulate Matter with an aerodynamic diameter $< 1 \mu\text{m}$
POA	Primary Organic Aerosol
	Summation of BBOA and FFOA
	Growth factor
GFR_{exBC}	The number concentration ratio between of externally mixed BC particles within total BC-containing particles

Externally mixed BC particles are defined as identified bare/thinly coated BC-containing particles at particle size of 200, 250, 300 and without humidification and is linked to aerosol hygroscopicity 370 nm

SA

Secondary Aerosols, including nitrate, sulfate, ammonium and the two OOA factors

Shrinkage Factor

SF

The ratio between particles with and without heating and is linked to aerosol volatility

PDF_{SIA}

Probability Distribution Function Secondary Inorganic Aerosols, including nitrate, sulfate, and ammonium

NF_H

Number Fraction of Hydrophilic aerosol whose hygroscopicity parameter is > 0.07

NF_V

Number Fraction of Volatile aerosol whose Shrinkage Factor at 200 °C is < 0.85

NF_{noBC}

Number Fraction of black carbon (BC) free particles

NF_{CBC}

Number Fraction of thickly coated BC particles

R_{exBC}

The number concentration ratio of externally mixed BC particles in total BC-containing particles

Externally mixed BC particles are defined as identified bare/thinly coated BC-containing particles

NF_A - NF_B

$(NF_{noBC} - NF_H - NF_V - NF_H - NF_{noBC} - NF_V - MAF - NF_{noBC} - MAF)SOA$

The difference between the number fraction of A and B Secondary Organic Aerosols, including the two OOA factors

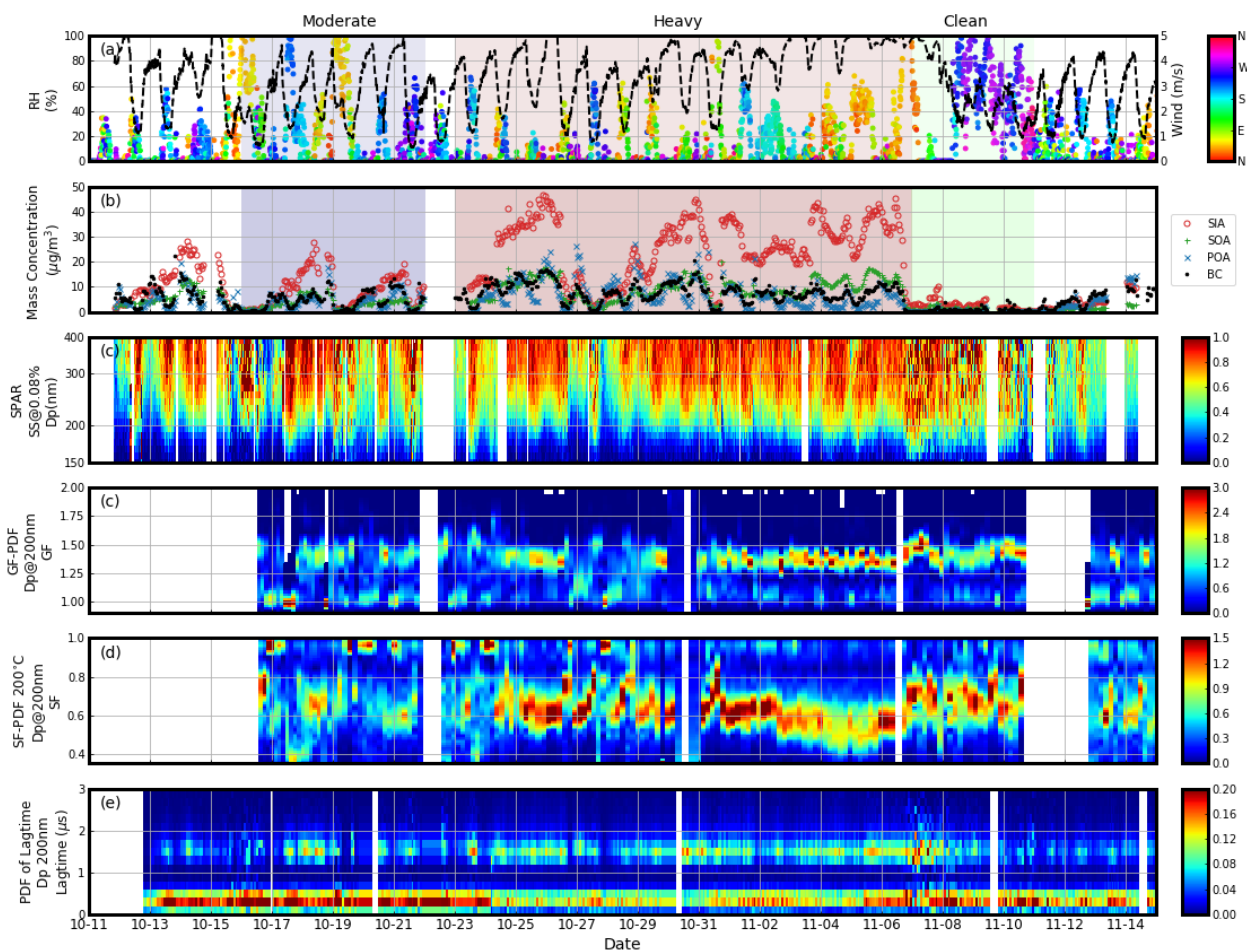
SPAR

Size-resolved Particle Activation Ratio

Size-dependent CCN activity under a specific SS

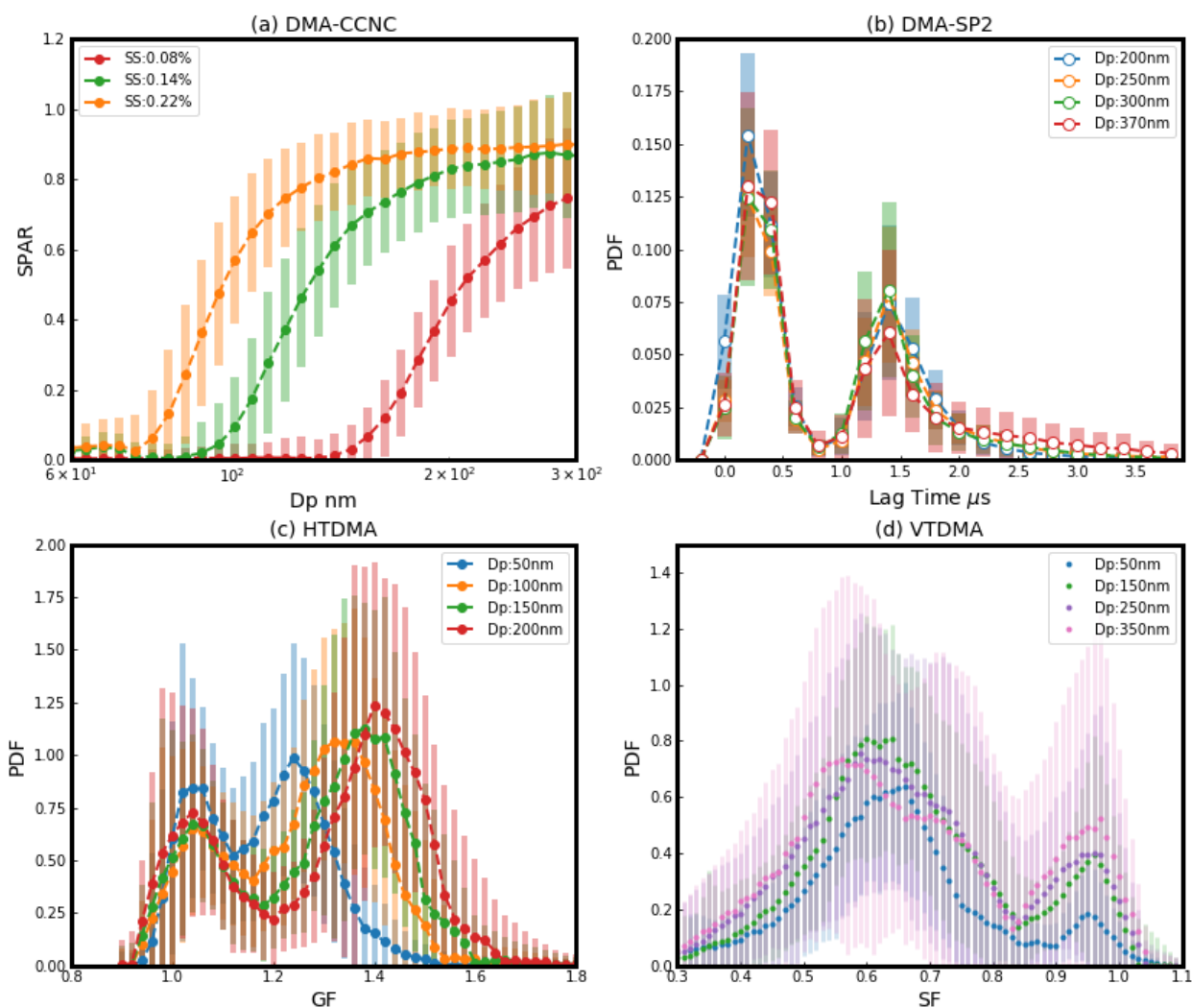
1237

1238



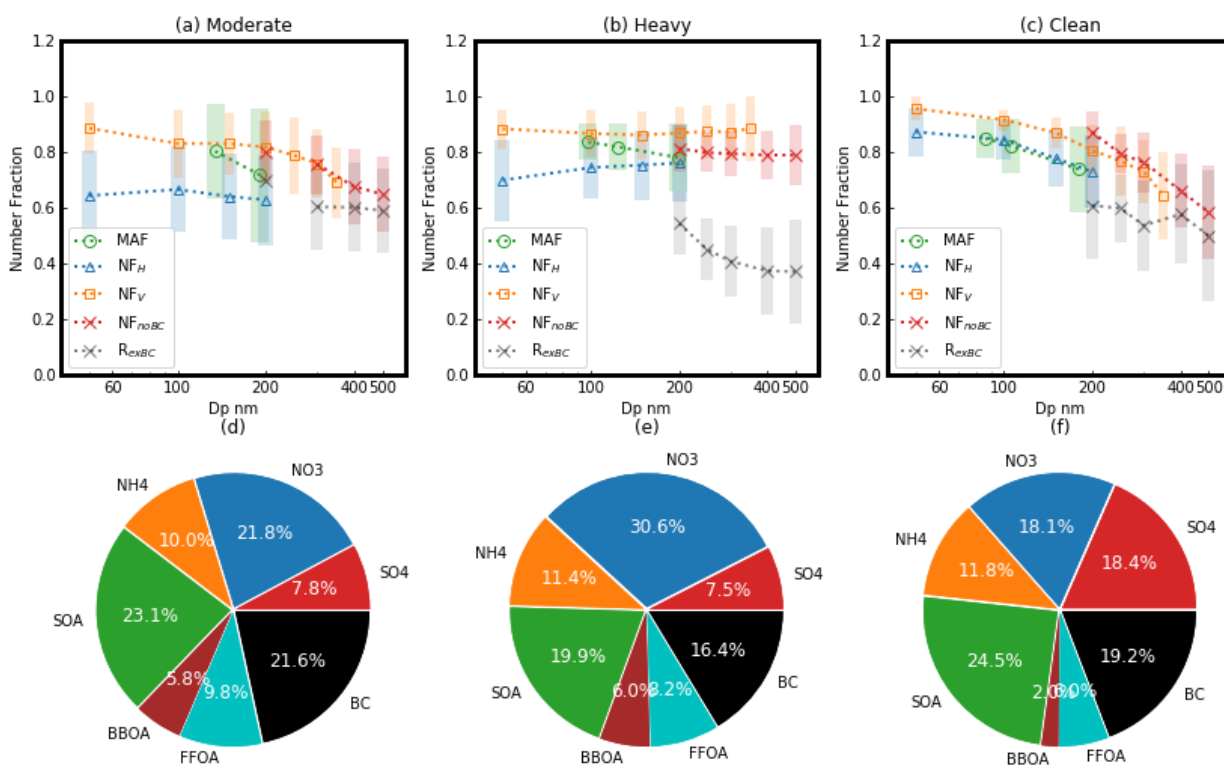
1239

1240 **Figure 1.** Overview of the measurements during the campaign: **(a)** meteorological parameters: wind speed (dots) and
 1241 relative humidity (RH) (black line), with colors of dots representing wind direction; **(b)** mass concentrations of
 1242 aerosol chemical ~~compositions~~ components: secondary inorganic aerosols (SIA, red circle), secondary organic
 1243 aerosols (SOA, green plus), primary organic aerosols (POA, blue x) and black carbon (BC, black dots); **(c)** Size-
 1244 resolved Particle Activation Ratio (SPAR) under supersaturation (SS) of 0.08% observed by the DMA-CCNC, with
 1245 warmer colors corresponding to higher values; **(d)** Probability Density Function (PDF) of growth factor (GF-PDF)
 1246 at 200 nm observed by the HTDMA; **(e)** PDF of shrinkage factor (SF-PDF) at 200 nm and 200 °C observed by the
 1247 VTDMA; **(f)** PDF of lag time at 200 nm observed by the DMA-SP2. The blue, red, and green shaded periods represent
 1248 the three periods with moderate pollution, heavy pollution, and clean conditions, respectively.



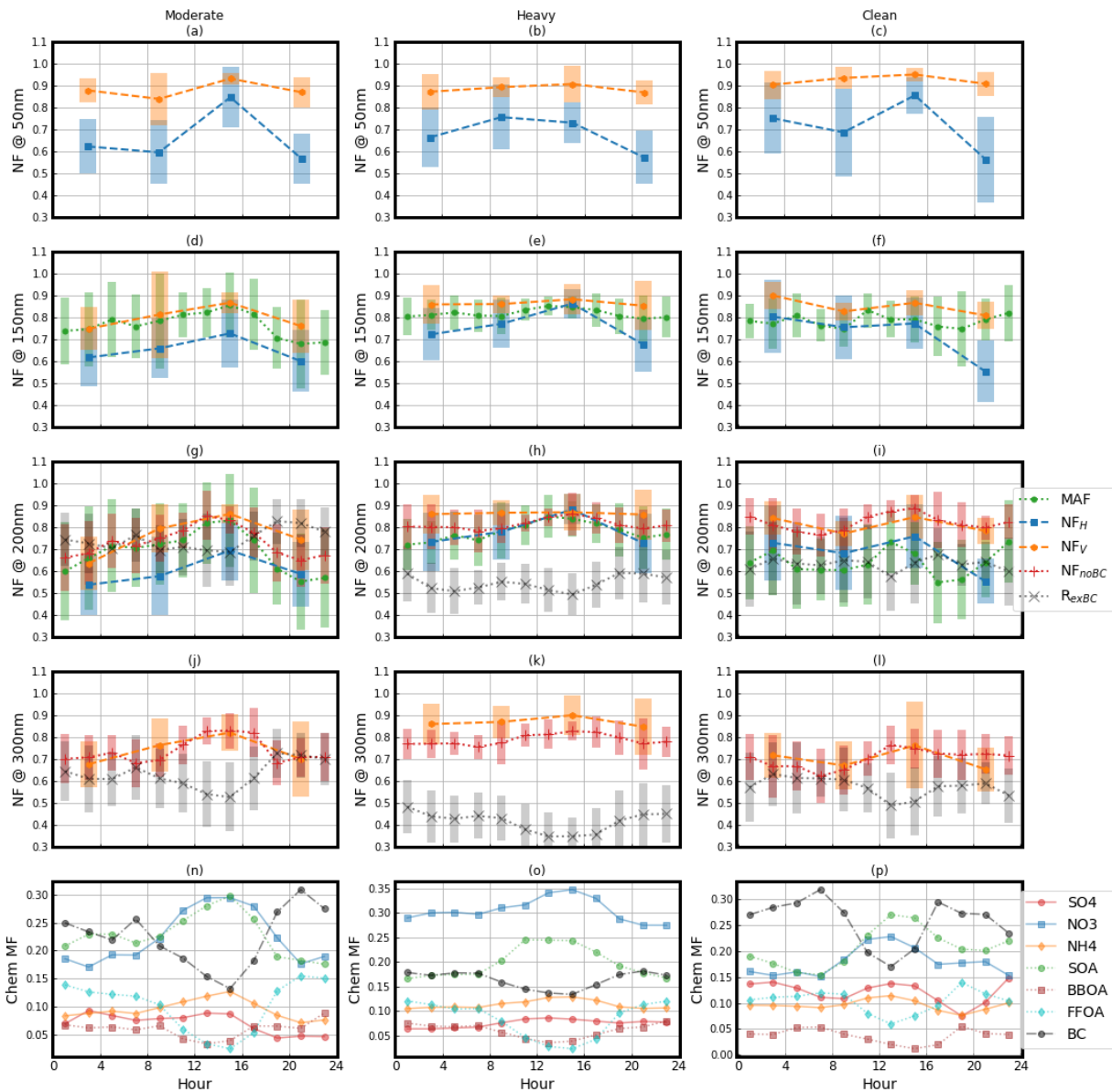
1249

1250 **Figure 2.** The campaign average of **(a)** Size-resolved Particle Activation Ratio (SPAR) curves measured by DMA-
 1251 CCNC at the three supersaturations (SSs, represented by different colors and markers), **(b)** Probability Density
 1252 Function (PDF) of lag time measured by DMA-SP2 at four particle sizes (represented by different colors and
 1253 markers), **(c)** PDF of growth factor (GF) measured by HTDMA at four particle sizes (represented by different colors and
 1254 markers), **(d)** PDF of shrinkage factor (SF) measured by VTDMA under the temperature of 200 °C at five particle
 1255 sizes (represented by different colors and markers). The shaded areas indicate the standard deviations.



1256

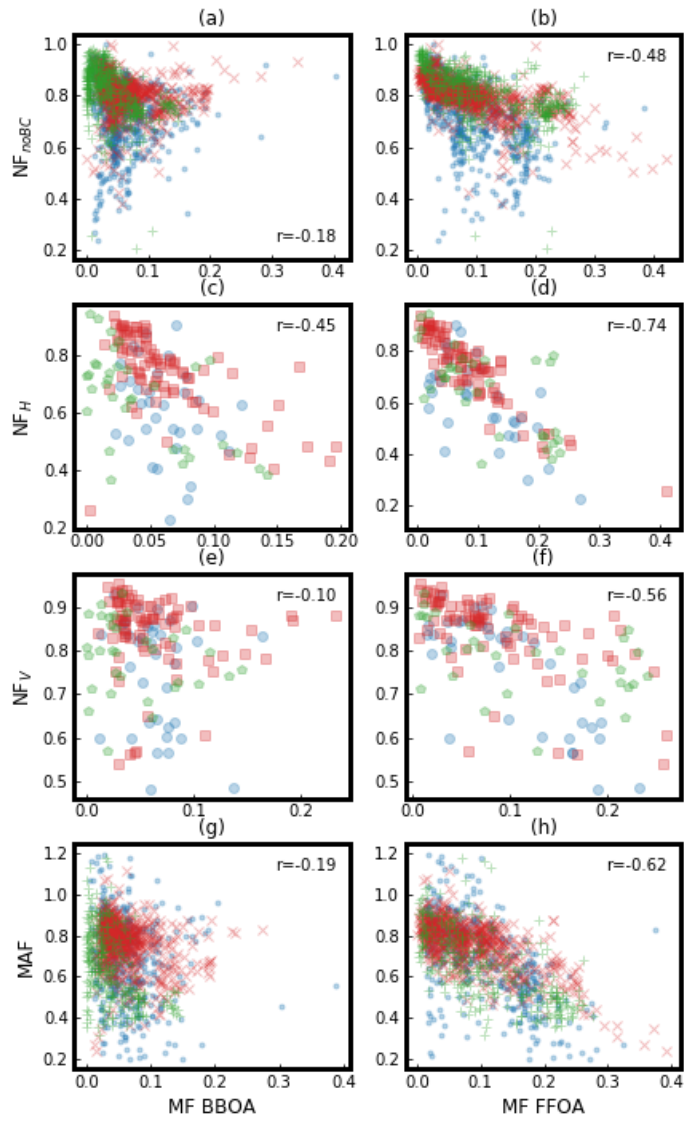
1257 **Figure 3. (a–c)** Size dependence of MAF (green circle), NF_H (blue triangle), NF_V (yellow square), NF_{noBC} (red x),
 1258 and R_{exBC} (black x) during the three periods. **MAF**: Maximum Activation Fraction, an asymptote of the measured
 1259 Size-resolved Particle Activation Ratio (SPAR) curve at large particle. **NF_H** : Number Fraction of Hydrophilic aerosol
 1260 whose hygroscopicity parameter is higher than ~ 0.07 . **NF_V** : Number Fraction of Volatile aerosol whose Shrink Factor
 1261 at $200^\circ C$ is lower than 0.85. **NF_{noBC}** : Number Fraction of black carbon (BC)-free particles. **R_{exBC}** : Number fraction
 1262 of externally mixed BC particles in total BC-containing particles. **(d–f)** Corresponding mass fractions (MFs) of
 1263 aerosol chemical compositions (identified by colors) during the three periods, including secondary
 1264 organic aerosols (SOA), biomass burning organic aerosol (BBOA), fossil fuel organic aerosols (FFOA), and inorganic
 1265 ions including sulfate (SO_4), nitrate (NO_3), and ammonium (NH_4).

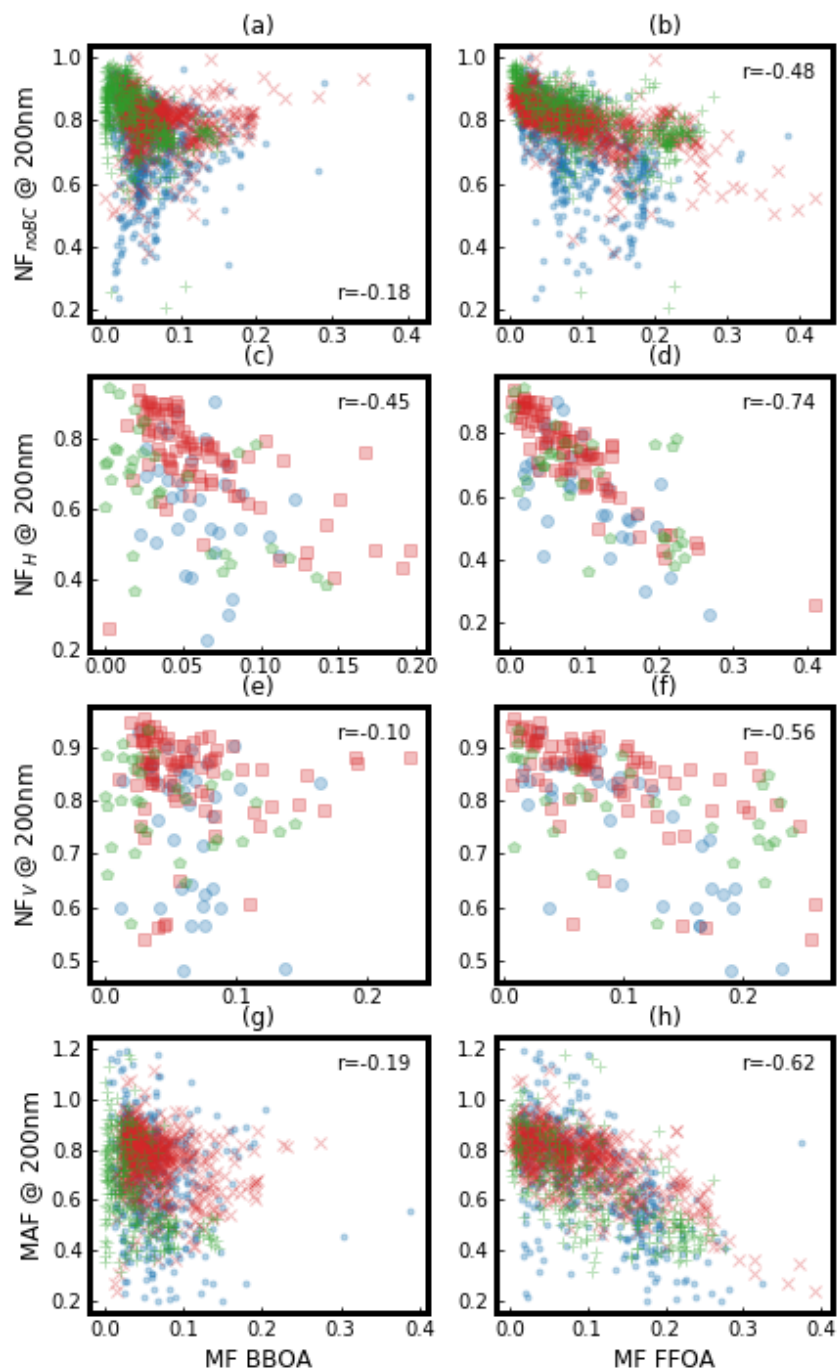


1266

1267 **Figure 4. (a–l)** Diurnal variations of aerosol mixing state parameters (identified by color and marker) at different
 1268 particle sizes (50, 150, 200, and 300 nm) during the three periods. The shaded areas indicate the standard deviations.
 1269 **(m–o)** Diurnal variations of mass fractions (MFs) of aerosol chemical ~~compositions~~ components, including secondary
 1270 organic aerosols (SOA), biomass burning organic aerosol (BBOA), fossil fuel organic aerosols (FFOA), and inorganic
 1271 ions including sulfate (SO₄), nitrate (NO₃), and ammonium (NH₄) (identified by color and marker) during the three
 1272 periods.

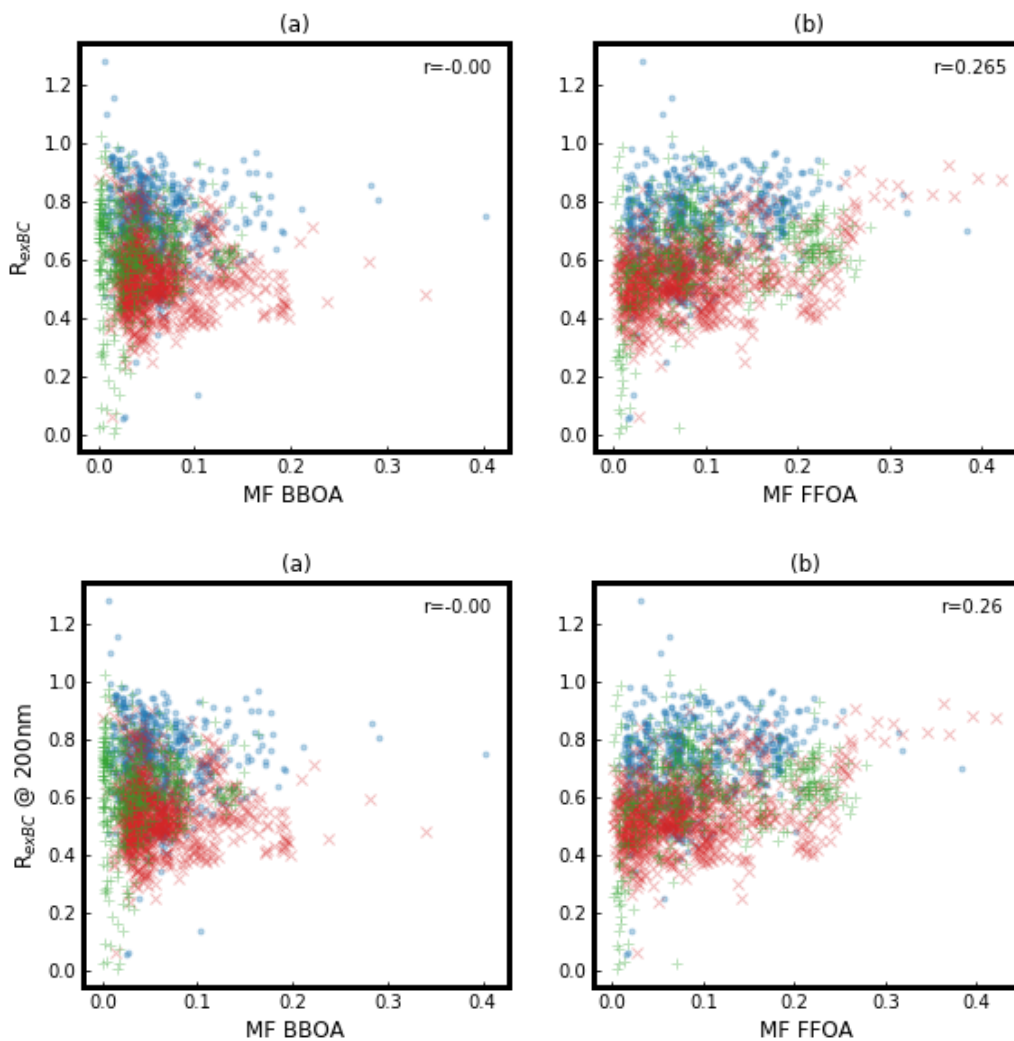
1273





1275

1276 **Figure 5.** The correlations between aerosol mixing state parameters and mass fractions (MFs) of biomass burning
 1277 organic aerosol (BBOA) and fossil fuel organic aerosols (FFOA) during different periods (moderately polluted period:
 1278 blue dot or circle; heavily polluted period: red x or square; clean period: green plus or pentagon), with r representing
 1279 the correlation coefficient.

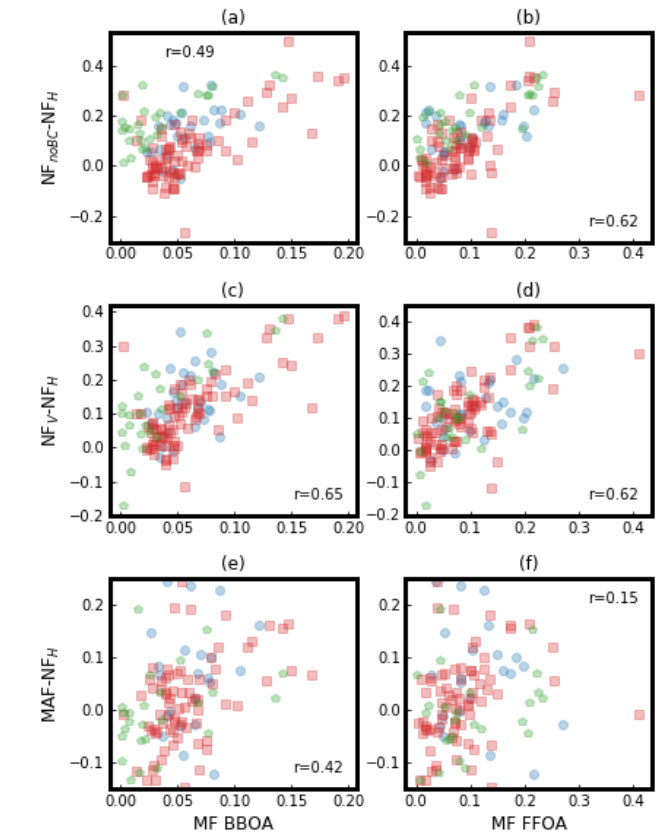


1280

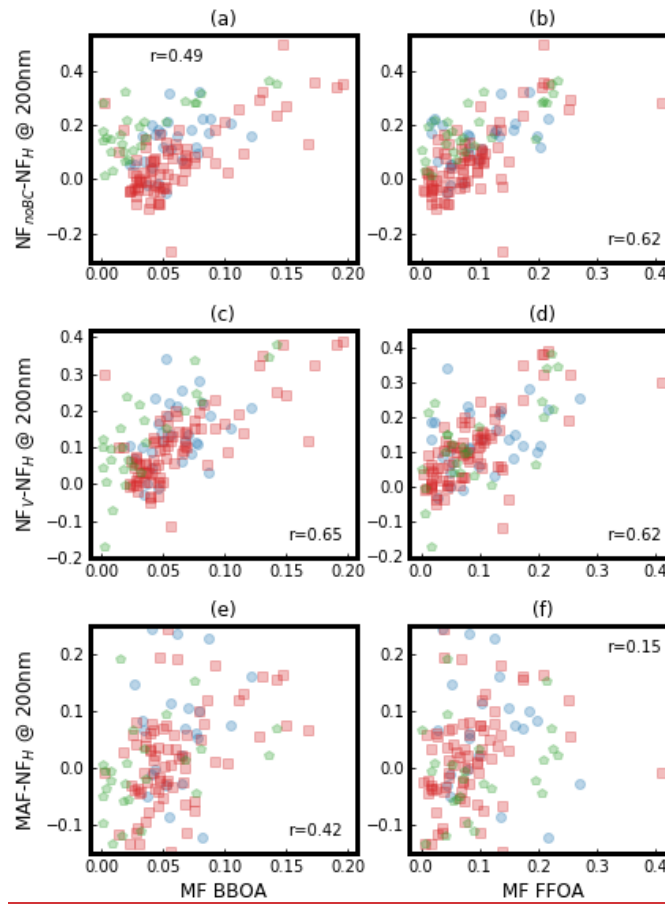
1281

1282 **Figure 6.** The correlations between the ratio of externally mixed black carbon (BC) in total BC particles (R_{exBC}) and
 1283 mass fractions (MFs) of biomass-burning organic aerosol (BBOA) and fossil fuel organic aerosols (FFOA) during
 1284 different periods (moderately polluted period: blue dot; heavily polluted period: red x; clean period: green plus), with
 1285 r representing correlation coefficient.

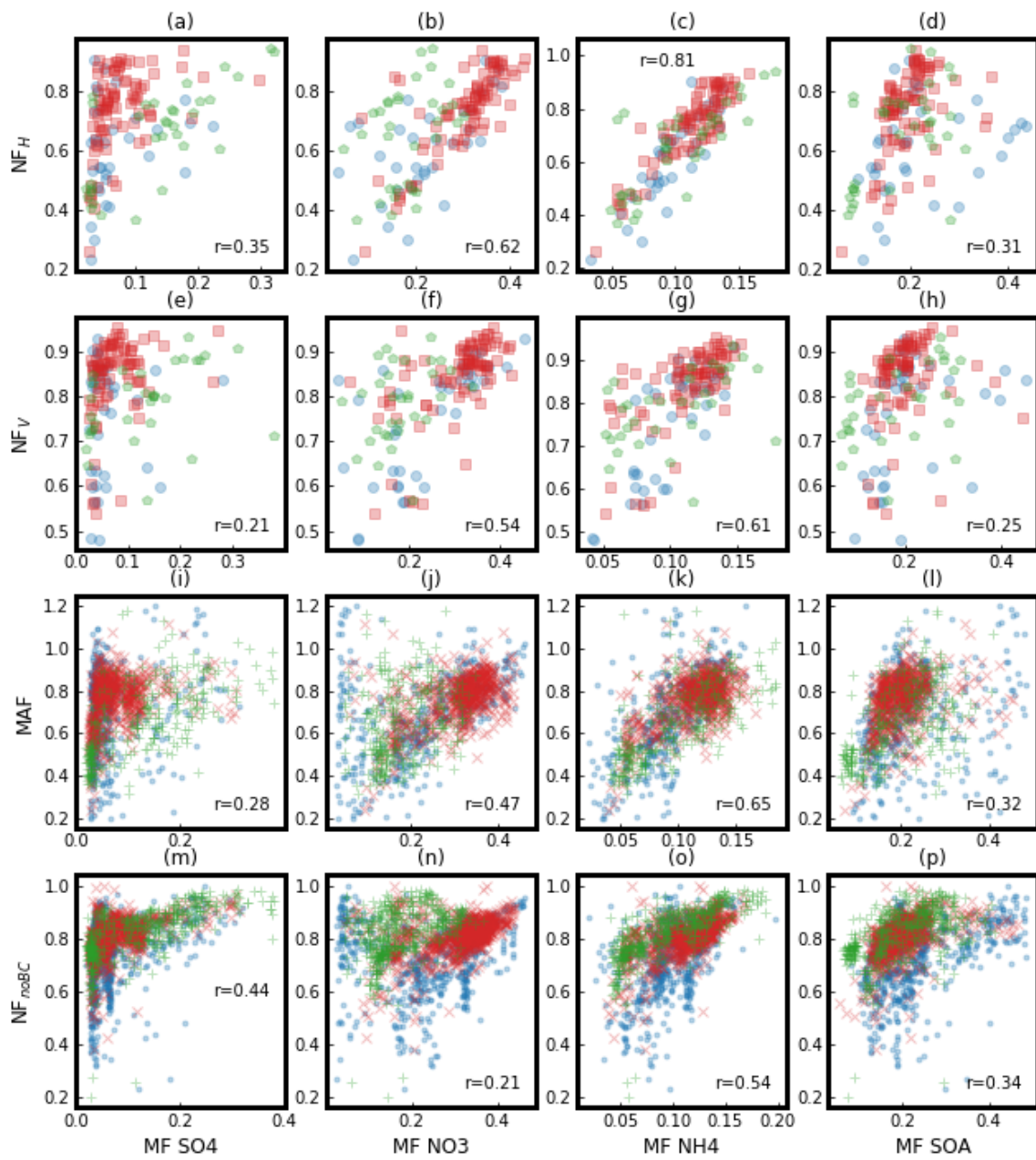
1286

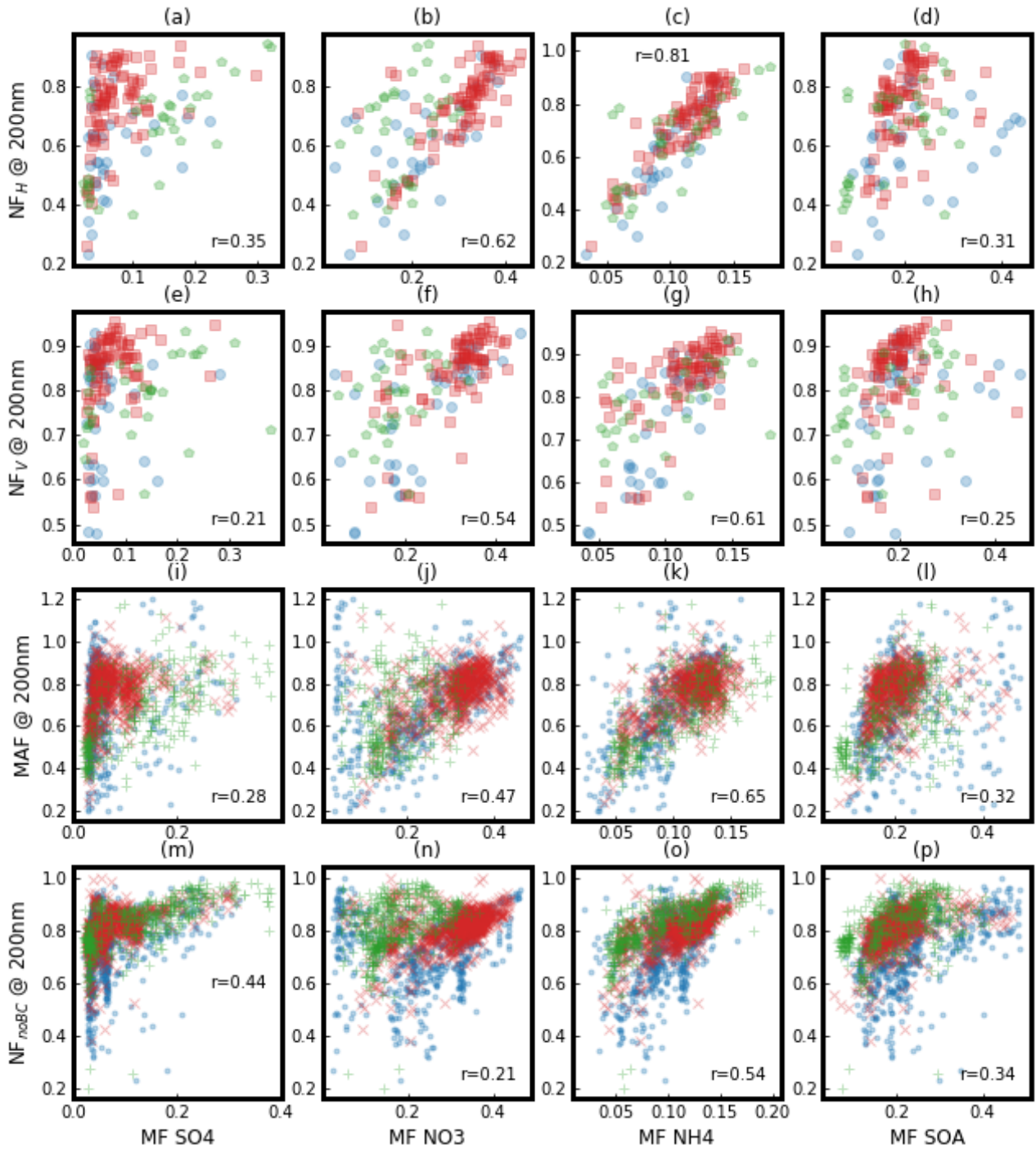


1287



1288 **Figure 7.** The correlations between the difference among the four aerosol mixing state parameters at particle size 200
1289 nm and mass fractions (MFs) of biomass burning organic aerosol (**BBOA**) and fossil fuel organic aerosols (**FFOA**)
1290 during different periods (moderately polluted period: blue circle; heavily polluted period: red square; clean period:
1291 green pentagon), with r representing correlation coefficient.





1293

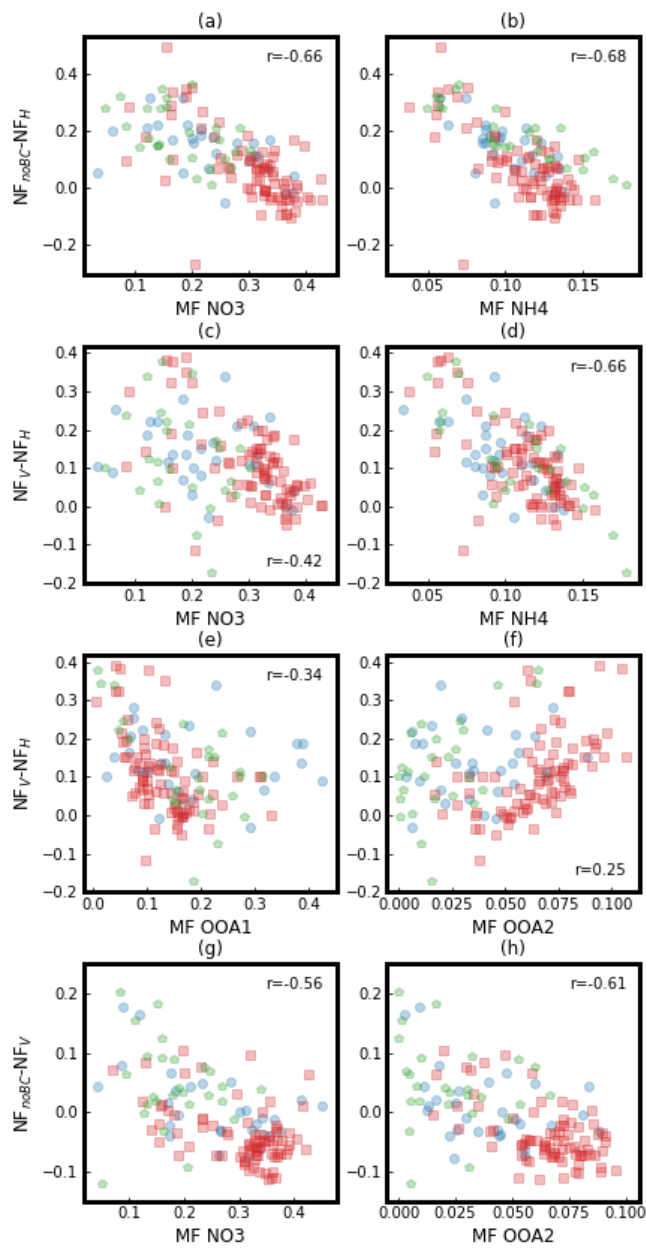
1294

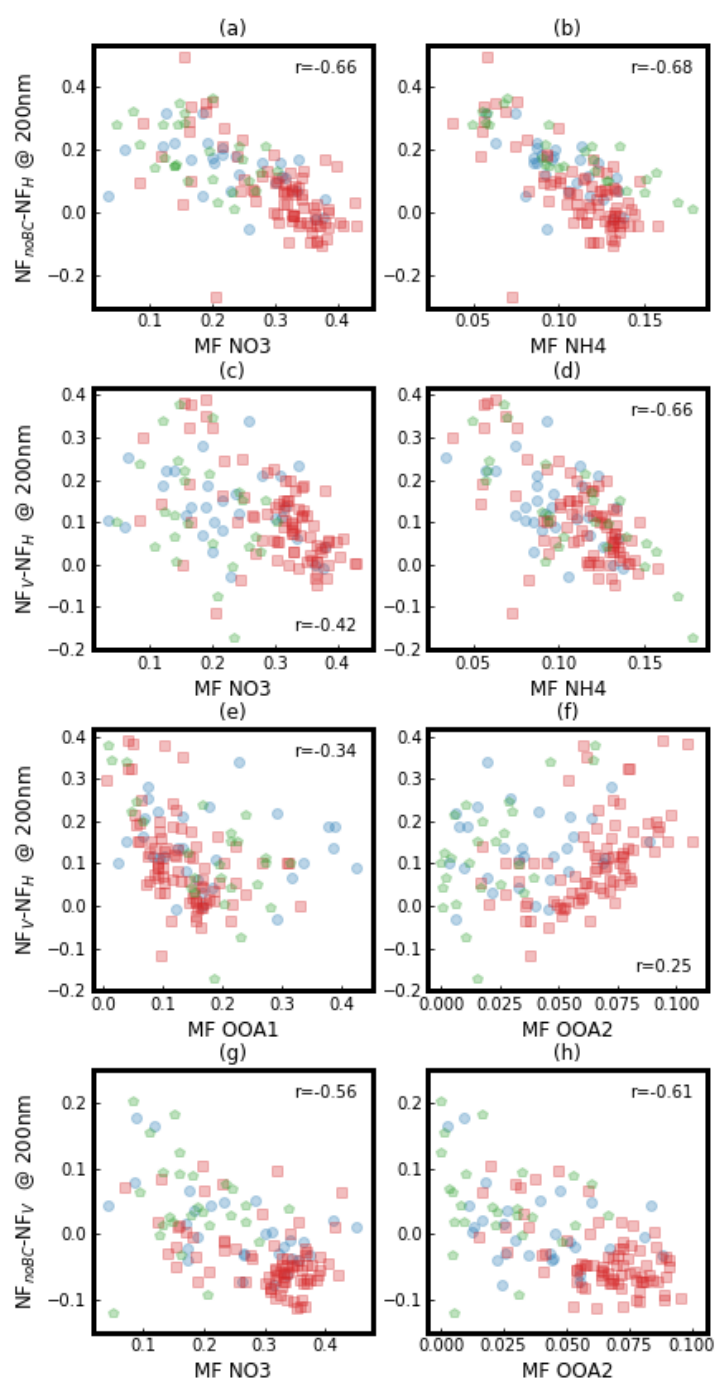
1295

1296

1297

Figure 8. The correlation between the four aerosol mixing state parameters and mass fraction (MF) of secondary aerosol (SA) components during different periods (moderately polluted period: blue dot or circle; heavily polluted period: red x or square; clean period: green plus or pentagon), with r representing correlation coefficient. SA components include secondary organic aerosols (SOA), sulfate (SO₄), nitrate (NO₃), and ammonium (NH₄)

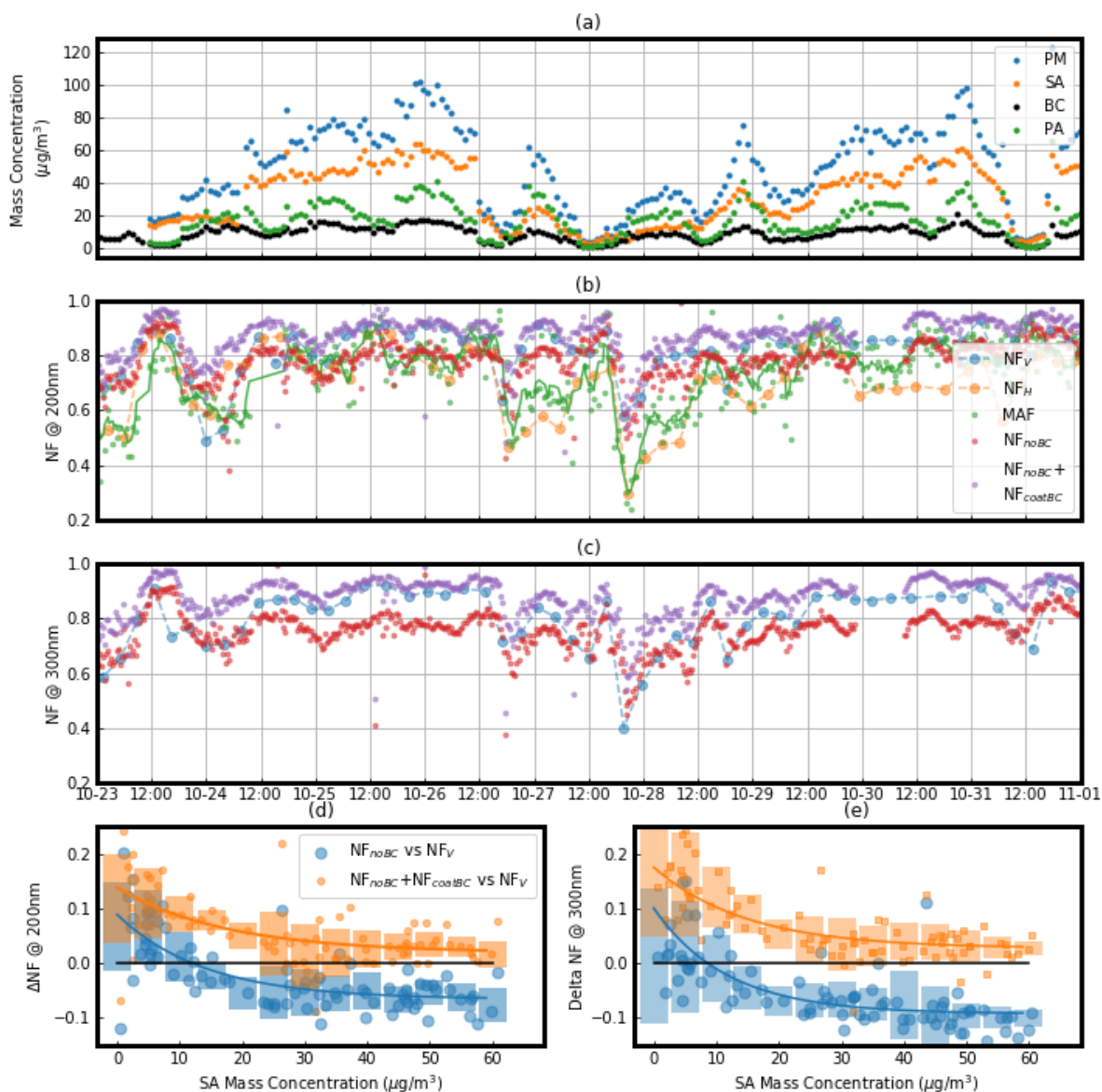




1299

1300
1301
1302
1303
1304

Figure 9. The correlation between the difference among the four aerosol mixing state parameters and mass fraction (MF) of secondary aerosol (SA) chemical components during different periods. OOA1 and OOA2 are two secondary organic aerosol (SOA) factors resolved from aerosol mass spectrometer (AMS) measurements using the Positive Matrix Factorization (PMF) technique. Moderately polluted period: blue circle; heavily polluted period: red square; clean period: green pentagon.



1305

1306

1307

1308

1309

1310

1311

1312

1313

1314

Figure 10. Variations of different aerosol mixing state parameters during the pollution accumulation process. **(a)** The time series of mass concentrations of non-refractory PM_{10} (NR- PM_{10}), secondary aerosols (SAs) (including inorganic ions and secondary organic aerosols (SOA)), primary organic aerosols (POA) and black carbon (BC) (identified by colors and markers). **(b and c)** The variations of different aerosol mixing state parameters (identified by colors and markers) at particle size 200 nm **(b)** and 300 nm **(c)**. **(d and e)** The variations of the difference between NF_V and NF_{noBC} ($\text{NF}_V - \text{NF}_{noBC}$, blue large circle) and the difference between NF_V and $\text{NF}_{noBC} + \text{NF}_{coatedBC}$ ($\text{NF}_V - (\text{NF}_{noBC} + \text{NF}_{coatedBC})$, yellow small circle) with the mass concentration of SA at particle size 200 nm **(d)** and 300 nm **(e)** $\text{NF}_{coatedBC}$: Number Fraction of thickly coated black carbon (BC) particles.